The Astrophysical Journal, 947:18 (20pp), 2023 April 10 https://doi.org/10.3847/1538-4357/acc529

Investigating the Effect of Solar Ambient and Data Characteristics on Ca II K Observations and Line Profile Measurements

M. Murabito[1], I. Ermolli[2], T. Chatzistergos[3], S. Jafarzadeh[3,4], F. Giorgi[2], and L. Rouppe van der Voort[4,5]
[1] INAF Osservatorio Astronomico di Capodimonte, Salita Moiariello 16, I-80131 Naples, Italy; mariarita.murabito@inaf.it
[2] INAF Osservatorio Astronomico di Roma, Via Frascati 33, I-00078 Monte Porzio Catone, Italy
[3] Max Planck Institute for Solar System Research, Justus-von-Liebig-Weg 3, D-37077 Göttingen, Germany
[4] Rosseland Centre for Solar Physics, University of Oslo, P.O. Box 1029, Blindern, NO-0315 Oslo, Norway
[5] Institute of Theoretical Astrophysics, University of Oslo, P.O. Box 1029, Blindern, NO-0315 Oslo, Norway
Received 2023 January 31; revised 2023 March 14; accepted 2023 March 15; published 2023 April 14

Abstract

We analyzed state-of-the-art observations of the solar atmosphere to investigate the dependence of the Ca II K brightness of several solar features on spectral bandwidth and spatial resolution of the data. In particular, we study data obtained at the Swedish Solar Telescope with the Crisp Imaging Spectropolarimeter and Chromospheric Imaging Spectrometer instruments. The analyzed data, which are characterized by a spectral bandwidth of 0.12 Å and a spatial resolution of 0.″078, were acquired close to the disk center by targeting a quiet-Sun area and an active region. We convolved the original observations with Gaussian kernels to degrade their spectral bandwidth and spatial resolution to the instrumental characteristics of the most prominent series of Ca II K observations available to date. We then studied the effect of data degradation on the observed regions and on parameters derived from Ca II K line measurements that are largely employed as diagnostics of the solar and stellar chromospheres. We find that the effect of degrading the spectral resolution of Ca II K observations and line profiles depends on both the employed bandwidth and observed solar region. Besides, we found that the spatial degradation impacts the data characterized by a broad bandwidth to a larger extent compared to those acquired with a narrow band. However, the appearance of the observed solar regions is only slightly affected by the spatial resolution of data with bandwidths up to 1 Å and in the range [3,10] Å. Finally, we derived relationships that can be used to intercalibrate results from observations taken with different instruments in diverse regions of the solar atmosphere.

Unified Astronomy Thesaurus concepts: Solar chromosphere (1479); Plages (1240); Solar photosphere (1518); Sunspots (1653); Solar activity (1475)

1. Introduction

Solar observations have often served as benchmarks of stellar conditions (Schmelz 2003; Engvold et al. 2019). A particularly illustrative example of the above link is given by the observations in the Ca II H and K lines at 3968.47 Å and 3933.67 Å, respectively, which are the two deepest and broadest absorption lines in the visible spectrum of the Sun.

In fact, early observations of the solar disk at the cores of the Ca II H and K lines revealed brightenings in large regions surrounding sunspots and in a network pattern across the whole solar disk (Hale & Ellerman 1903). Concurrently to these observations, late-type stars were also found to commonly show emissions at the Ca II H and K lines and thus considered to have atmospheric layers similar to those of the Sun (Eberhard & Schwarzschild 1913). Later on, solar observations revealed a clear association between brightening at the Ca II H and K lines and the magnetic field strength (Babcock & Babcock 1955; Howard 1959; Chatzistergos et al. 2019b) and area (Leighton 1959; Sheeley 1967). Along with previous observations, this association allowed the Ca II H and K emissions to be used as an indicator of the magnetic fields in the Sun and other stars (Wilson 1978). Since then, measurements at the Ca II H and K lines have been widely used to trace changes in the surface of the Sun and other stars due to magnetic activity and other processes such as rotation and convection (e.g., White & Livingston 1978; Baliunas 1984; Keil & Worden 1984; Noyes et al. 1984; Baliunas et al. 1995; Hall et al. 1995; Radick et al. 1998; Hall et al. 2007; Radick et al. 2018, and references therein).

Furthermore, for many years, the Ca II H and K lines have been used as one of the most reliable diagnostics of the physical properties of the solar (Linsky 1970; Linsky & Avrett 1970) and stellar (Linsky 2017) chromospheres. This is due to the characteristic profile of the Ca II H and K lines, which show two peaks and two secondary minima toward the violet or red part of the spectrum relative to the line center, and a reversal at the line center. These line features result from emissions originating from the photosphere, where the temperature decreases with height until a temperature minimum is reached, to the overlying lower chromosphere, where the temperature increases with height (Linsky 1968). Following the notation given by Hale & Ellerman (1903), in the Ca II K line the abovementioned line features are labeled as K_{1V}, K_{1R}, K_{2V}, K_{2R}, and K_3, respectively. It is noteworthy that they all occur within a 1 Å interval and are qualitatively the same for both the quiet-Sun and plages regions. However, for the latter the K_{2V} and K_{2R} peaks and the K_3 minimum display a significant intensity increase relative to the quiet Sun (Linsky 1970).

It is worth noting that, although both spectral regions are observable from the ground, the Ca II H and K lines have not been equally explored, with existing observations in favor of

the Ca II K line. Contributing to this is that the Ca II H line is blended with the Balmer Hϵ line at 3970.07 Å. Another reason is that Ca II H line is slightly less sensitive than Ca II K as an atmospheric diagnostic. This is because the Ca II H emission peaks are often less pronounced than in the Ca II K ones, thus probing lower heights in the chromosphere. Further information on the formation and diagnostic potential for the solar atmosphere of the Ca II H and K lines can be found in, e.g., Linsky (1970) and Bjørgen et al. (2018).

The literature concerning solar and stellar observations at the Ca II K line is extensive and suggestive of plenty of data available at that radiation. In fact, full-disk spatially resolved solar observations at the Ca II K line have continuously been performed since 1892 with various telescopes operating at the Ca II K line with bandwidths in the range [0.09,10] Å centered at the line core, and spatial resolution larger than 1″ (e.g., Chatzistergos et al. 2018, 2019a, 2020, 2022a). Most prominent archives of historical Ca II K data are, e.g., those of the Meudon (Malherbe et al. 2022), Kodaikanal (Chatzistergos et al. 2019c), Mt Wilson (Lefebvre et al. 2005), and Coimbra (Lourenço et al. 2019) Observatories, while the ones for modern data are, e.g., those of the Rome (Ermolli et al. 2022) and Kanzelhöhe (Pötzi et al. 2021) Observatories. In addition, since the late 1960 s the Ca II K line emission integrated over the solar disk has been measured almost daily at, e.g., the Kitt Peak and Sacramento Peak sites of the US National Solar Observatory (e.g., White et al. 1998; Scargle et al. 2013) and at the Kodaikanal Observatory in India (e.g., Sivaraman et al. 1987). Furthermore, there are also Ca II K observations at high spectral resolution, on the order of 0.2 Å or better, acquired on spatially resolved regions of the solar disk with a spatial resolution even better than 0.″2, but over limited time intervals and disk positions. Such data are, e.g., those obtained over the last few years at the Swedish Solar Telescope, which are further described in the following.

In addition to the observations described above, since the 1960s the disk-integrated Ca II K emission of the Sun and late-type stars has been monitored at the Mt Wilson Observatory (1966–2003, Wilson 1978; Duncan et al. 1991; Baliunas et al. 1995), then at the Lowell Observatory (1994–present, Hall et al. 2007), and more recently with the Potsdam Echelle Polarimetric and Spectroscopic Instrument (PEPSI) of the Large Binocular Telescope (LBT; see, e.g., Dineva et al. 2022), with the High Accuracy Radial velocity Planet Searcher North spectrograph at the Telescopio Nazionale Galileo (TNG; see, e.g., Maldonado et al. 2019), and with the photometers on board, e.g., the Convection Rotation and planetary Transits (CoRoT; Michel et al. 2008; Auvergne et al. 2009; Gondoin et al. 2012) and Kepler (Borucki et al. 2010; Koch et al. 2010) missions.

It is worth noting that, in spite of being widely observed over many years, several aspects of the Ca II H and K emissions in the atmosphere of the Sun and other stars are still not fully understood. Examples are the link between the coverage of a stellar disk by magnetic features and the Ca II H and K emissions (see, e.g., Sowmya et al. 2021), and the relationship between Ca II H and K brightening and magnetic field strength (see, e.g., Chatzistergos et al. 2019b). These gaps in the knowledge of the Ca II H and K emissions depend on several factors. First, all the available observations report relative photometric data with respect to some standard that is subjective of a biased definition. For example, the disk-resolved solar observations carry information of the brightening at the Ca II K line with respect to an average quiet-Sun emission, whose definition depends on the data characteristics and their processing methods. Likewise, the disk-integrated measurements describe line parameters with respect to a continuum reference that is hardly identified in the solar and stellar spectra adjacent to the Ca II H and K lines, because of the presence of many absorption lines. Unfortunately, the various observations that are available in the literature have often been obtained with diverse instruments and methodologies, which render their comparative analysis inconclusive.

We aim to contribute to a better knowledge of the Ca II H and K emissions, in particular of the relationship between Ca II K emission and magnetic field strength. As a first step, here we investigate the dependence of the Ca II K line data on different ambient conditions of the solar atmosphere due to different levels of magnetic flux, and characteristics of the observations, by using state-of-the-art data taken at the solar disk center.

The paper is structured as follows. In Section 2 we describe the data analyzed in our study and the methods used to process them. In Section 3 we present our results on the measured Ca II K emissions depending on the spectral and spatial resolution of the analyzed observations. We discuss our results and summarize them by drawing our conclusions in Sections 4 and 5, respectively.

2. Data and Methods

2.1. Observations

The data analyzed in our study were acquired at the Swedish 1 m Solar Telescope (SST; Scharmer 2006) with the CRisp Imaging SPectropolarimeter (CRISP; Scharmer et al. 2008) and with the CHROMospheric Imaging Spectrometer (CHROMIS; Scharmer 2017) at the Fe I doublet lines at 6301.51–6302.50 Å (hereafter 6301–6302 Å) and the Ca II K line at 3933.67 Å (hereafter 3933 Å), respectively. In particular, we analyzed three series of simultaneous full-Stokes Fe I and Stokes-I Ca II K observations acquired close to the disk center by targeting a quiet-Sun area (QS) and an active region (AR), namely, AR NOAA 12585. The CRISP and CHROMIS data are characterized by an image scale of ≈0.″060 pixel^{-1} and 0.″039 pixel^{-1}, and a spectral resolution of about 60 mÅ and 120 mÅ, respectively, over a field of view (FoV) of about $1' \times 1'$.

The QS data were acquired on 2017 May 25 from 08:06 to 11:16 UT at $\mu = 0.99$, by targeting a region with patches of regular and irregular granulation, hereafter referred to as quiet-Sun granulation (QG) and quiet-Sun magnetized granulation (QM), respectively. The QS data consist of several scans of full-Stokes Fe I and Stokes-I Ca II K measurements. The Fe I line data were taken sequentially at nine spectral positions around the Fe I 6301 Å line center, at six spectral positions around the Fe I 6302 Å line center, and at −0.26 Å from the Fe I 6302 Å line center for the continuum, by referring to the rest-frame line centers. The Ca II K data were taken at 41 equally spaced positions in the range [−1.30,+1.30] Å relative to the line center and at 4000 Å for the reference continuum measurement. The cadence was 19.6 s and 13.6 s for Fe I and Ca II K, respectively.

The AR data were acquired on 2016 September 5 from 09:48 to 10:07 UT at $\mu = 0.99$, by targeting a sunspot (SP) with umbral (UM) and penumbral (PE) regions and a neighboring area (NA) with plages (PL) and several pores (PO),

respectively. Similarly to the QS set, the AR data include several series of full-Stokes Fe I measurements and Stokes-I Ca II K data. Here the Fe I doublet lines were sampled as described above for the QS observations, while the Ca II K line measurements were obtained at the following 21 spectral positions: [−1.4, −0.78, −0.70, −0.63, −0.55, −0.47, −0.39, −0.23, −0.16, −0.08, 0., +0.08, +0.16, +0.23, +0.39, +0.47, +0.55, +0.63, +1.25] Å relative to the line center, i.e., on a slightly smaller spectral range than that used for the QS data, and at 4000 Å as the reference continuum. The Fe I and Ca II K data sets were taken at cadence of 32 s and 14 s, respectively.

The data analyzed in our study were extracted from all the observations available for the QS, NA, and SP regions, as the best frames among the 20 nonconsecutive observations of each solar target that are characterized by the highest contrast for best seeing during their acquisition.

The QS, NA, and SP observations have been previously studied by Bose et al. (2019), Murabito et al. (2021), and Esteban Pozuelo et al. (2019), respectively.

2.2. Data Reduction

The data analyzed in our study were reduced by using the CRISPRED (de la Cruz Rodríguez et al. 2015) and CHROMISRED (Löfdahl et al. 2021) pipelines for the CRISP and CHROMIS data, respectively. The processing consists of several steps, including among others application of bias and flat-field response of the detectors, compensation for spatial variation in the spectral instrumental response, for optics aberrations, and for atmospheric turbulence with the Multi-Object Multi-Frame Blind Deconvolution (MOMFBD; Löfdahl 2002; van Noort et al. 2005) image restoration. The latter step compensates for residual seeing degradation over the FoV unaccounted for by the adaptive optic system of the SST.

The data produced by the above pipelines were further processed as follows. First, they were derotated to account for diurnal field rotation. Then we aligned the CRISP and CHROMIS data and reduced them to the same pixel scale, by using as reference the frames acquired at the Fe I 6302 Å Stokes-I line continuum and Ca II K continuum at 4000 Å, which both originate in the low photosphere. In particular, we scaled up the CRISP data to the pixel scale of the CHROMIS data. This was done to maintain the original resolution of the Ca II K observations. Then, we rotated the CRISP images and trimmed them to match the FoV of the corresponding CHROMIS images. We used a cross-correlation technique to apply vertical and horizontal image shifts that result in a close match at subpixel accuracy. The above processing led to images that cover a region of about $50'' \times 40''$ for each target, with images having slightly different dimension of 1369×1066, 1367×1004, and 1403×1067 pixels^2 for the QS, NA, and SP data sets, respectively.

Figure 1 shows examples of the spectral-line profiles extracted from the data obtained from the processing described above. In particular, we show the sampling of Ca II K 3933 Å line resulting from spatial averaging of the data over the whole FoV of the QS set (red dots), depicted on the full spectra (solid line) from the disk-center atlas measurements from Delbouille et al. (1973)[6] for the sake of clarity. The data are normalized to the intensity of the reference continuum. We note that the spatially averaged Ca II K spectra are slightly higher for QS than the reference. This could be due to the analyzed FoV.

Figure 1 makes it clear that the available Ca II K data only probe the Ca II K line center with its typical double reversal and the innermost part of the line wings, but they do not sample the extended Ca II K line wings away from the line center that sample the deeper layers of the photosphere.

To account for these characteristics of the data we applied the following processing steps. First we performed the absolute wavelength and intensity calibration of the Ca II K observations. Due to the different shape of the profiles measured in the QS regions with respect to the ones measured in NA and SP areas[7] we used, as reference, the solar disk-center atlas data by Delbouille et al. (1973) for the QS observations, and the sunspot umbral spectra from Wallace et al. (2005)[8] for the NA and SP observations. Then, we extrapolated the analyzed data to cover a wider spectral range than the one of the measured values, by using the atlas measurements at several spectral positions in the line wings as a reference. In particular, we assumed that the values extrapolated for the measured series follow the ones in the atlas at the following spectral positions [3916.9, 3924.0, 3929.6, 3932.4, 3935.0, 3939.5, 3942.1, 3949.3] Å for the QS observations, and at the following spectral positions [3924.0, 3929.6, 3932.4, 3935.0, 3939.5, 3942.1, 3949.3] Å for the NA and SP observations. It is worth noting that these positions were selected after performing several tests and trials aimed at optimizing the results obtained, while the slightly different spectral positions considered for the QS and other sets derive from the fact that the measurements of the atlas umbral spectra are only available for wavelengths larger than 3920.5 Å.

We used results from linear interpolations between pairs of the above reference positions to reconstruct values of an extrapolated line profile that mimic the behavior of emission in the Ca II K line wings. However, we note that the data obtained by combining the measured and extrapolated values simulate high-resolution spectral observations of the Ca II K line center and low-resolution spectral observations of line wings, the latter without accounting for the many lines that populate the spectra adjacent to the Ca II K line center. We further consider this limitation of the data obtained from our processing in the following.

Finally, we applied spectral and spatial degradation to the data obtained from the previous processing steps, by convolving them with Gaussian kernel functions of varying width, in order to investigate the effect of spectral bandwidth and spatial resolution of the data on Ca II K observations and line measurements of various solar features. In particular, we convolved the CHROMIS observations, which were taken with a 0.12 Å spectral bandwidth, with 1D Gaussian functions with a FWHM of [0.2, 0.3, 0.4, 0.5, 0.6, 0.7, 1.0, 1.8, 2.5, 3.0, 5.0, 10.0] Å. These spectral widths (hereafter referred to as bandwidths and spectral degradations) match the bandwidths of most of the existing series of full-disk solar observations at the Ca II K (see, e.g., Tables 1 and 2 in Chatzistergos et al. 2022b). Moreover, we convolved the original data (with a spatial sampling of $0''.039$ pixel^{-1}) with a spatial 2D Gaussian kernel with a FWHM of [$0''.18$, $0''.3$, $1''.0$]. This spatial degradation was to represent the spatial resolution of the

[6] Available at the BASS2000 Archive. https://bass2000.obspm.fr

[7] The different shape is mostly in terms of the line width close to the line center.

[8] Available at https://nispdata.nso.edu/ftp/pub/atlas/spot4atl/.

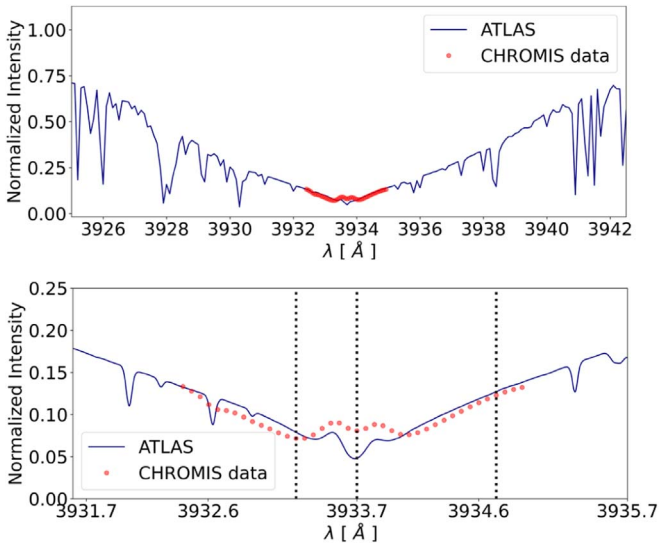

Figure 1. Examples of CHROMIS spectral sampling (red dots) of the Ca II K line 3933 Å. The measurements refer to a QS region and are normalized to the data at the reference continuum (not shown). Overplotted are disk-center atlas measurements (blue solid line) from Delbouille et al. (1973). Vertical dotted lines mark the spectral samplings of the Ca II K observations shown in Figure 2.

photospheric and chromospheric observations acquired with SUNRISE's Imaging Magnetograph eXperiment (SUNRISE/IMaX; Solanki et al. 2010; Barthol et al. 2011; Martínez Pillet et al. 2011; Solanki et al. 2017), Hinode's Solar Optical Telescope (Hinode/SOT; Ichimoto et al. 2008; Tsuneta et al. 2008), and SDO's Helioseismic Magnetic Imager (SDO/HMI; Pesnell et al. 2012; Scherrer et al. 2012; Schou et al. 2012), respectively. We note that, at present, the data from the above instruments are the most widely employed for studies of the photosphere and chromosphere. In addition, we also investigated the full-disk solar observations produced with a moderate spatial resolution resulting from a pixel scale larger than $2''$ pixel^{-1}. As mentioned above, these observations have been regularly obtained at several observatories since the beginning of the 20th century. We note that the instance of these observations is interesting in light of the role they play in connecting series of historical and modern full-disk solar Ca II K line observations (Chatzistergos et al. 2022b). In this case we convolved the original CHROMIS data with a spatial 2D Gaussian kernel with a FWHM of $4''$.

On both the original observations and data obtained from the above processing (i.e., the degraded data), we then evaluated two observable parameters of the Ca II K line that are widely employed for the monitoring of the chromosphere on the Sun and late-type stars. In particular, following, e.g., Scargle et al. (2013), Bjørgen et al. (2018), and Dineva et al. (2022), we estimated the K_3 intensity in the Ca II K line core and the emission index equivalent width in the 1 Å band centered on the line profile (hereafter referred to as EMDX). Indeed, among the various Ca II K line parameters employed in the literature, K_3 and EMDX are the most sensitive to changes in the Ca II K line profile. We computed K_3 by measuring the intensity at 3933.67 Å and EMDX by integrating the data with the five-point Newton–Cotes integration formula of the *int_tabulated* function in the *Interactive Data Language (IDL)*.

3. Results

Figure 2 shows examples of the observations analyzed in our study. In particular, we show the data taken at the Fe I 6302 Å line continuum (panels (A)–(C)), in the Ca II K line core (panels (D)–(F)), at roughly the secondary minimum K_{1V} in the violet wing of the Ca II K line (panels (G)–(I)), and in the red wing of the line at +1.05 Å from the line core (panels (J)–(L), for the QS (left-column panels), NA (middle column panels), and SP (right-column panels) regions. We show the observations of the same solar features at the above diverse positions along the Ca II K line in order to highlight their different appearances as is in the case of the data of some existing series of Ca II K solar observations, e.g., the set of the Meudon Observatory that includes data at the center and blue wing of the Ca II K line.

The photospheric Fe I data of the three observed regions show the regular granulation pattern in QS areas (panel (A)), elongated granules around the pores (panels (B)), and other larger-scale features, such as the umbra and penumbra (panel (C)) in the SP target including bright umbral dots and dark and bright filaments, respectively. The Ca II K line core images display the chromosphere above the same areas, consisting of thin bright and dark fibrils everywhere, except in the umbra and inner part of the penumbra, and of several localized bright features (panels (D)–(F)). On the other hand, the data taken at the K_{1V} and in the red wing of the Ca II K line display disk features typical of the upper photosphere and temperature minimum, namely, the reversed granulation pattern and the bright features in the intergranular lanes that are due to magnetic field concentrations and/or acoustic grains (panels (G), (J)). These patterns are more evident in the red wing observations. Umbral regions are dark in all Ca II K observations, while in line core and line wing data penumbral areas are only partially so (panels (F), (I), (L)). We note extended brightenings may also appear in the umbral regions (in the chromosphere) due to umbral flashes. The pores are dark in line wing observations (panels (H)–(K)), while line core data display small-scale (transient) brightening at higher atmospheric heights above them (panel (E)). All the Ca II K images show brightness patterns due to granulation and associated with dark magnetic features. Most of the bright/dark fibrils in the core images seem to overlie the bright patches displayed by the wing images (panels (D), (G), (J) and panels (E), (H), (K)). The fibrils observed in the Ca II K line core data are only slightly curved.

It is worth noting that the diverse solar regions described above are characterized by rather different Ca II K line profiles and are only representatives of the regions sampled in these observations that could look different based on, e.g., other magnetic topology. In Figure 3 we compare the Ca II K line profiles obtained from spatial averaging of the Ca II K line data in quiet areas of the QS, NA, and SP regions, overplotted on the high-resolution spectrum from the atlas of Delbouille et al. (1973). Similarly to the latter, all the profiles derived from the observations show the K_{1V} and K_{1R} secondary minima in the violet and red part of the spectrum, respectively, the reversed line center K_3, and the two K_{2V} and K_{2R} peaks, with K_{2V} stronger than K_{2R} as reported in the literature. The above line features are almost inappreciable on the top right panel of the figure resulting from the QS observations, but they increase significantly in the data from SP regions (bottom right panel).

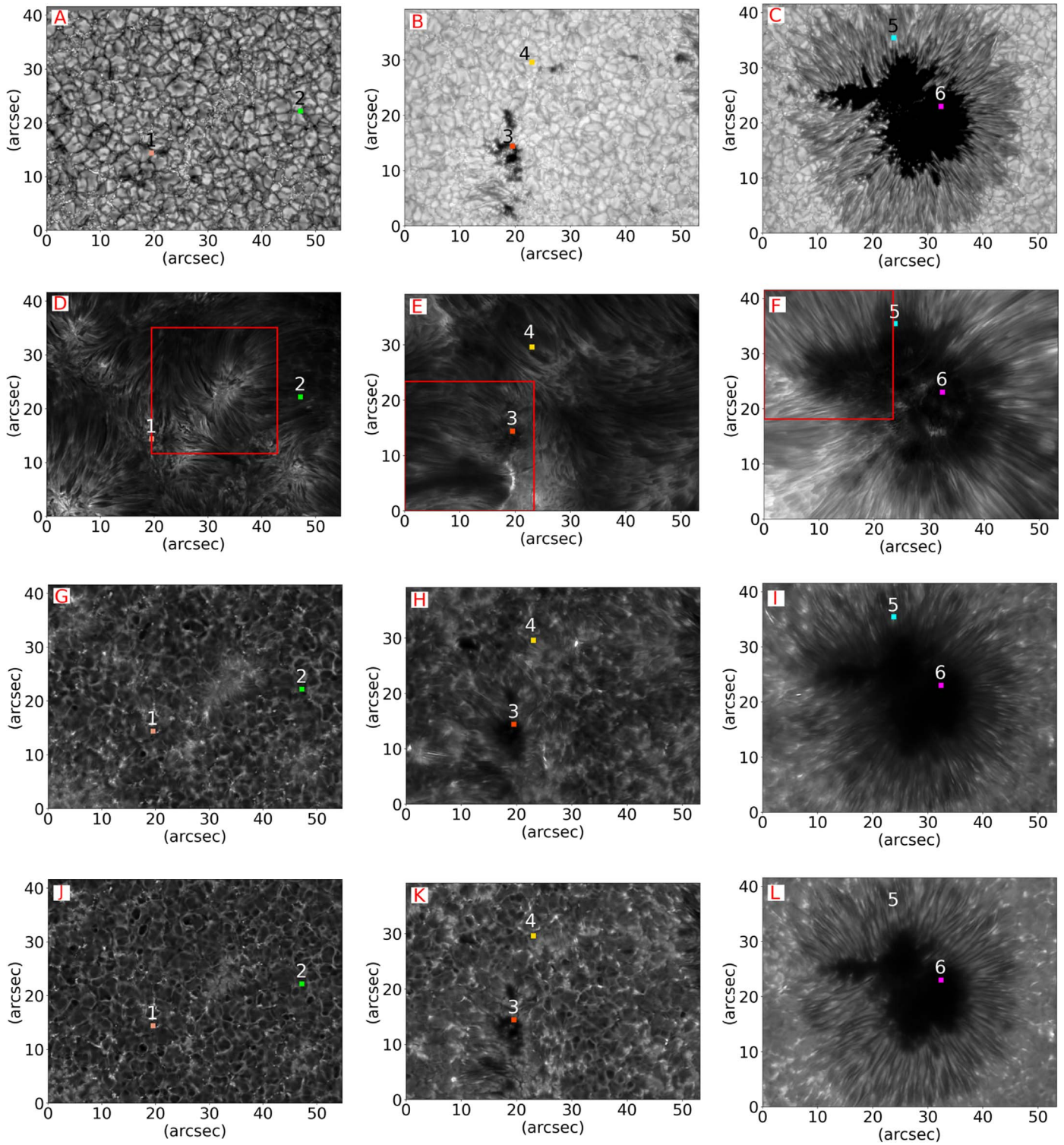

Figure 2. CRISP Fe I 6302 Å continuum images (panels (A)–(C)) and CHROMIS Ca II K 3933 Å images in the line core (panels (D)–(F)), at −0.42 Å from the line core at roughly K_{1V} (panels (G)–(I)), and at +1.05 Å in the red wing (panels (J)–(L)) of the three regions analyzed in our study, referring to a quiet-Sun area (left-column panels), an active region with plages and several pores (middle column panels), and a sunspot with umbra and penumbra (right-column panels). After the image processing described in Section 2.2, the CRISP and CHROMIS observations are shown here with same dimension and pixel scale, which in the original data are in favor of the CHROMIS observations and is maintained here. Each observation is shown using the intensity interval that enhances the visibility of the solar features therein. The small colored boxes show the six 20 × 20 pixels wide areas randomly selected in the observations to represent the solar features analyzed in our study in the ambient to which they belong. The boxes are shown in all panels to make comparisons easier. The red boxes on the line core observations mark the regions shown in Figures 5, 7, and in Appendix B.

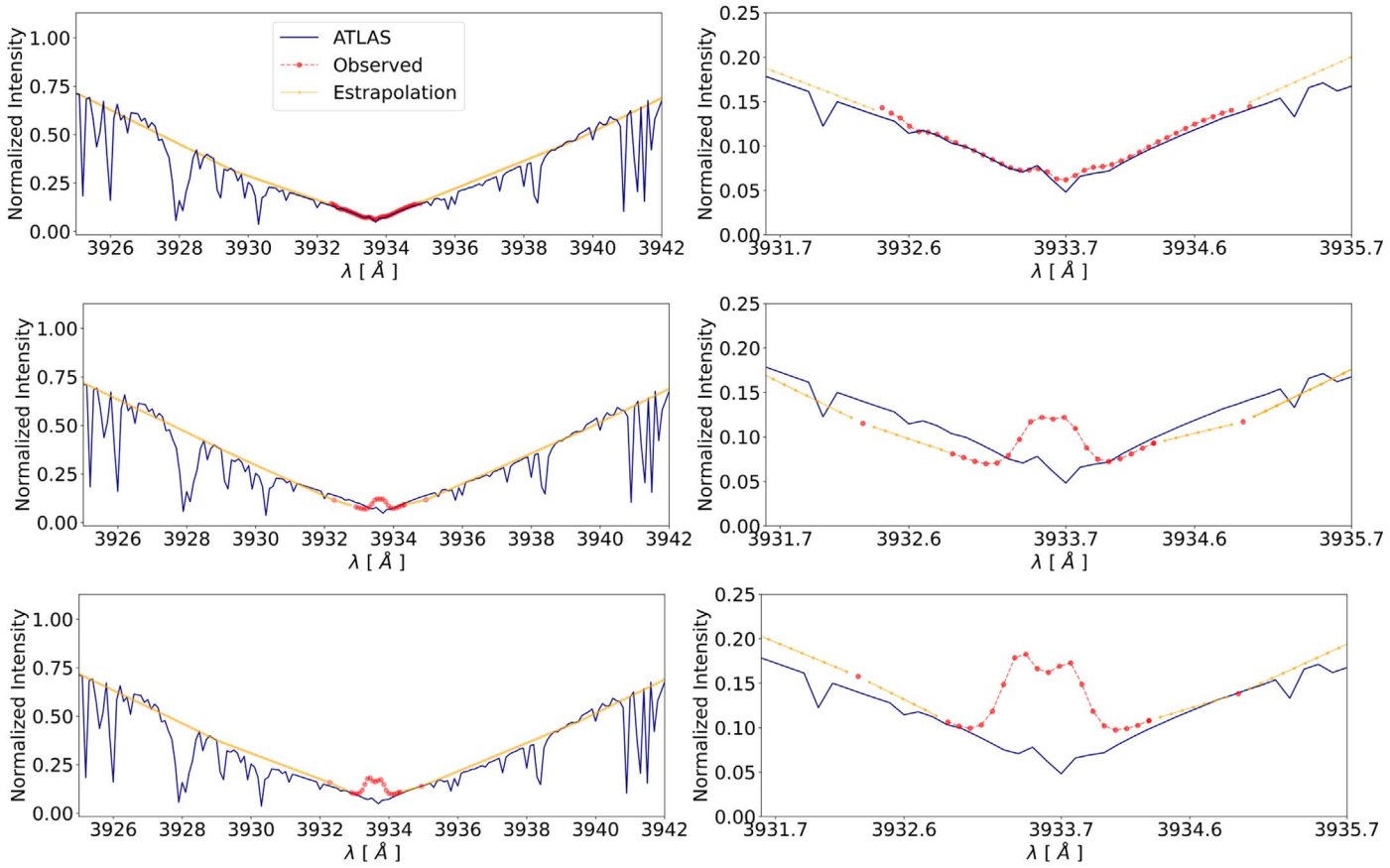

Figure 3. Examples of Ca II K line profiles analyzed in our study. These were obtained by averaging data in subarrays representative of quiet areas in the studied QS (top panels), NA (middle panels), and SP (bottom panels) regions. The values are normalized to the data at the reference continuum at 4000 Å (not shown). The blue profile and red dots in each panel indicate the atlas data from Delbouille et al. (1973) and our observations, respectively. The yellow line describes the results from the data extrapolation based on atlas values.

On the other hand, in the NA case the K_3 line center, and the two K_{2V} and K_{2R} peaks are not visible (middle right panel).

We notice that the separation of the line peaks and their width in all the QS spatially averaged observed profiles are close to the ones in the atlas profile. However, this is not the case for profiles extracted from individual pixels in the analyzed observations. Figure 4 displays some examples of these profiles, from the 20×20 pixels wide areas marked with numbers and colored boxes in the QS, NA, and SP observations of Figure 2. For each area under investigation, we also show the line profile (black solid line) derived from averaging the data available at each spectral position of our spatially resolved observations.

The profiles in Figure 4 show different characteristics: there are profiles with emission peaks significantly increased (QM box 1, top left panel) with respect to the ones in Figure 3, as well as profiles with fuzzy K_{2V} and K_{2R} peaks and a reversed strength than that reported in the literature (QG box 2, top right panel), and profiles lacking the K_3 minimum (PO box 3, middle left panel; PE box 5, bottom left panel; and UM box 6, bottom right panel).

We note that the profiles in Figure 4 are derived from the areas randomly selected to represent diverse solar features in the ambient to which they belong. Indeed, analyzing slightly different areas in their surroundings, the obtained profiles often retain the characteristics of the individual profiles in Figure 4, but this is not always the case. Besides, the mean profiles derived from other boxes nearby the ones in Figure 2 can slightly differ from the average profiles in Figure 4. This is particularly evident in results derived from QM and QG data. Some examples for these data are given in Appendix A.

3.1. Effect of Spectral Bandwidth

We wondered how the Ca II K observations and measured line profiles presented in the previous section are affected by the characteristics of the instruments employed for Ca II K measurements, in particular their spectral bandwidth and spatial resolution. To answer the above question, in Figure 5 we show an about $25'' \times 25''$ FoV of the original CHROMIS observations at the Ca II K line center for the three analyzed solar regions (panels A, E, I) and corresponding data after their spectral degradation with kernels having a FWHM of 1, 3, 10 Å (all other panels). The regions shown in Figure 5 are the ones marked with red boxes in Figure 2.

As expected, smearing the original data with a spectral kernel leads to the mixing of photospheric and chromospheric emissions. The fibrils filling the original QS FoV (panel (A)) are faintly detectable with a spectral degradation of 0.6 Å (not shown) and almost no longer seen with 1 Å bandwidth (panel B), which allows PO and UM regions to manifest themselves with spatial scales and intensities (panels (F), (J)) close to the ones displayed by the same features in images acquired with a spectral degradation of 3–10 Å (panels (G), (K) and panels (H), (L)). Observations of the QS region with such bandwidths show the reversed granulation and dot-like bright features

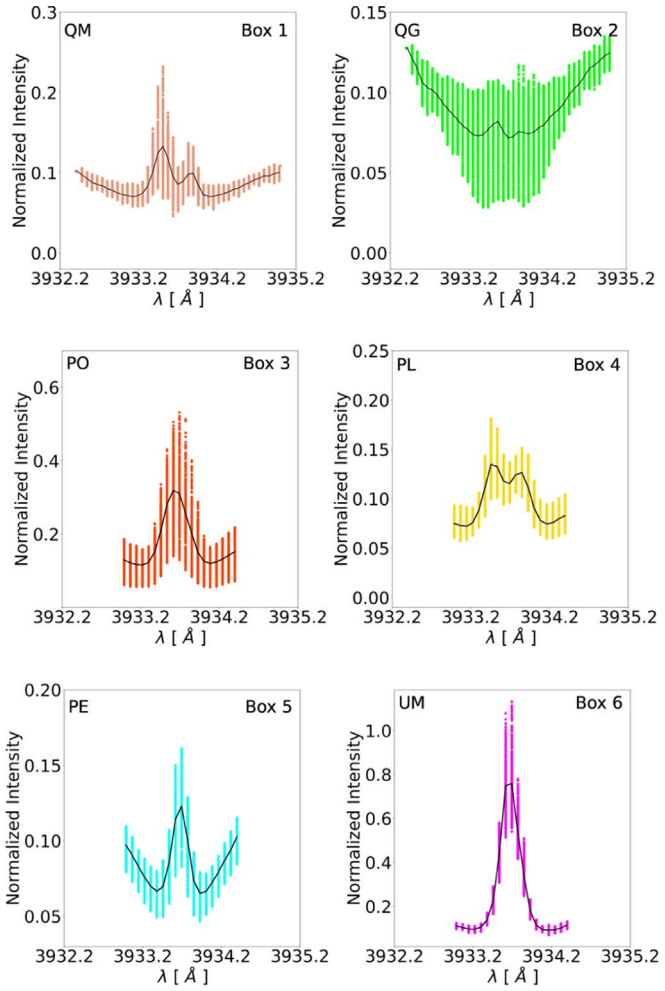

Figure 4. Examples of Ca II K line profiles analyzed in our study. These were obtained from the 20×20 pixels wide areas marked with numbered and colored boxes in Figure 2. Black solid lines show the mean profiles derived from the spatially resolved data available at each observed spectral position. We recall that the QS region (top row panels), to which the QM and QG areas belong, was sampled over a slightly larger spectral range than the NA (middle row panels) and SP (bottom row panels) regions, where the PO, PL, PE and UM areas were selected.

(panels (C)–(D)) seen in the original observations at the red wing of the Ca II K line (shown in Figure 2, panel (J)).

Among the three regions studied here, the NA target is the one visually showing the largest change in its appearance with the various spectral degradation kernels. This applies, in particular, to data obtained with bandwidths up to 1 Å and those derived from bandwidths in the range [3,10] Å. Indeed, the former data show fibrils similar to penumbral filaments, while in the latter data bright granular elements appear around the pores. These granular features, which seem to be raised above the pores, are outlined by thin dark boundaries, as reported in, e.g., Lites et al. (2004) from a study of SST photospheric data. The same features also resemble the patterns attributed to sea-serpent magnetic configurations in, e.g., Murabito et al. (2021). We also notice that the panels in Figure 5, illustrating spectrally degraded data, show brightness patterns with similar position and extension in QS observations (panels (B)–(D)), and partly so in the SP data (panels (J)–(L)). However, the average Ca II K brightening of disk features in the above degraded images is always lower than in original CHROMIS observations. We also note that degrading the observations with larger kernels leads to appearance of smaller-scale structures and finer details (panels (D), H, L), and reversed granulation pattern (panels (C)–(D)).

The above effect of spectral degradation of the data is even more evident when considering the Ca II K line profiles. In Figure 6 we show line profiles extracted from the original and spectrally degraded observations of the various targets in Figure 5. We report spatially averaged profiles computed over the regions marked with numbers and colored boxes in Figure 2.

Figure 6 shows that a spectral degradation on the order of 10 Å results in an increase in the K_3 intensity of the Ca II K line core, and of the intensity all along the line profile, in all the areas except in the UM one. On the other hand, a spectral degradation of only 2.5 Å results in an increase in the K_3 intensity in QM and QG areas, being more evident in the latter case, and a decrease of the same quantity in all the other targets. Noteworthy, spectral bandwidths from 0.7 to 2.5 Å have similar effects on the line profiles derived from the PO and PL areas.

Figure 6 also shows that the features of the Ca II K line typical of each studied areas disappear completely in observations characterized by a bandwidth of 1.8 Å. It is worth noting that this spectral bandwidth is lower than the ones used by most sites currently performing observations in the Ca II K line with optical filters, but higher than all the ones of spectroheliograph data (see Chatzistergos et al. 2022b).

We note that the various panels in Figure 6 also include shaded areas, which cover the range of values measured over each analyzed region. These shaded areas manifest the large heterogeneity of the Ca II K line profiles in the studied observations when considered at the spatial resolution of the CHROMIS observations. This heterogeneity is particularly evident in the QS data, which seem to be especially affected by intensity oscillations due to hydrodynamic pressure modes (p-modes; Leighton 1960), and very noticeable in the line wings, where small changes in wavelength due to p-modes lead to large variations in intensity. On the other hand, intensity fluctuations are also evident in the profiles derived from the NA areas, while they are not appreciable in the profiles obtained from the SP field. The intensity fluctuations in both these regions are most likely attributable to magnetohydrodynamical oscillations (MHD modes; e.g., Spruit 1982) and to small-scale transient brightening from magnetic reconnection events.

Overall, the results presented above suggest that the effect of spectral bandwidth on Ca II K line profiles depends on both the employed bandwidth and observed solar region.

3.2. Effect of Spatial Resolution

We then considered the impact of spatial degradation on our data. As an example, in Figure 7 we show data derived from spatial degradation of the original observations of the QS region, under the diverse spectral degradations analyzed above. For the sake of comparison, we also show the original CHROMIS observations, characterized by a spatial resolution of 0.″078. More examples for the QS, NA, and SP regions are given in Appendix B and presented in the following. For all these examples, we considered the spatial resolution of the SUNRISE/IMaX, Hinode/SOT, and SDO/HMI observations acquired with a pixel scale of 0.09, 0.15, and 0.″5 pixel^{-1}, respectively. Moreover, we considered the case of the synoptic full-disk observations characterized by a moderate pixel scale of 2″ pixel^{-1}, as in the data acquired at, e.g., the Rome Observatory. The results for the latter case are also reported in Appendix B.

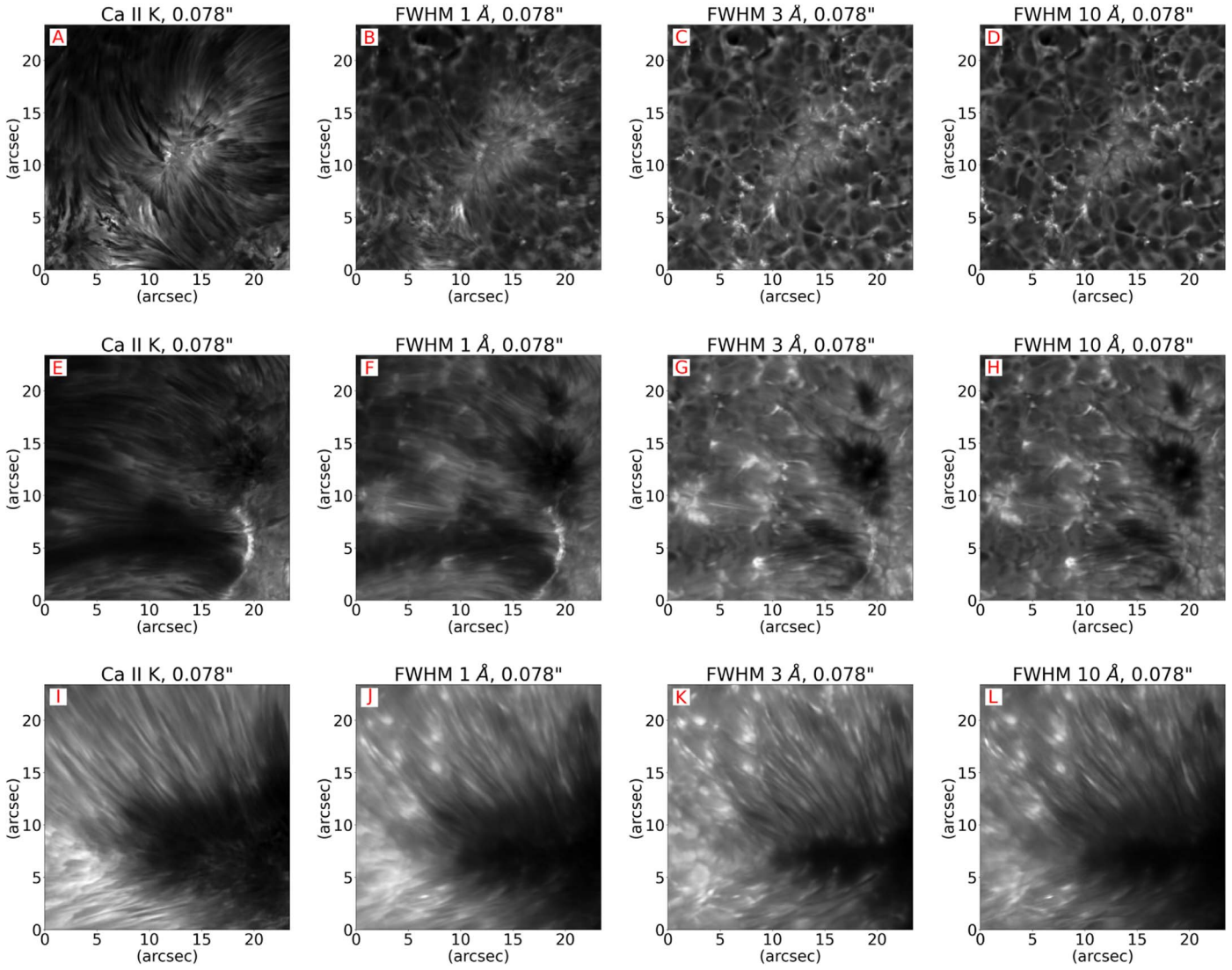

Figure 5. Examples of the observed (left-column panels) and spectrally degraded (all other panels) images at the Ca II K line core of the three studied solar regions, namely, a quiet-Sun area (top row panels), a region with plages and several pores (middle row panels), and a sunspot with umbra and penumbra (bottom row panels), all observed close to the disk center. For each target, from left to right we show original CHROMIS observations and data degraded with Gaussian kernels with a FWHM of 1, 3, and 10 Å. Each image is shown using the intensity interval that enhances the visibility of the solar features therein.

For the data representative of all the above pixel scales, we considered spectral degradations resulting from the application of Gaussian kernels with a FWHM of 1, 3, and 10 Å to the original CHROMIS data characterized by a 0.12 Å spectral resolution. The above FWHM values are distinctive of the bandwidth of optical filters employed for modern observations in the Ca II K line at, e.g., the Rome, Kanzelhöhe, and San Fernando Observatories.

From the data in Figure 7, we notice that the spatial degradation impacts almost equally the data characterized by a spatial resolution better than 0.″3. Besides, we observe that the appearance of the data is barely affected by employed spectral bandwidths in the range [1,10] Å. This also applies to data degraded to the 4″ spatial resolution typical of full-disk observations, which show the main features of the observed regions seen in the higher-resolution data preserved on larger spatial scales, and less details at the small scales. These findings are in agreement with the results reported by Chatzistergos et al. (2021) concerning reconstructions of irradiance variations and unsigned magnetograms derived from Ca II K observations, which both resulted to be only slightly sensitive to the bandwidth of the analyzed observations in the range [0.09,9] Å and to the data spatial resolution in the range of ∼[2,11]″.

As mentioned above, more examples of solar-region data at the original resolution of the CHROMIS observations and derived from the various degradation kernels applied to them are given in Appendix B. In particular, we show examples of the QS region observed in the red wing of the Ca II K line at +1.05 Å from the line core and of the NA and SP areas observed at the Ca II K line core. From these additional examples we note that, regardless of the spatial and spectral degradation applied to the data, the QS target shows different characteristics when observed in the Ca II K line core and in the red wing of the Ca II K line, but the latter resemble observations at the K_{1V}. On the other hand, we notice that the granular bright features surrounding the pores in the NA region observed at the Ca II K line core with the 0.″078 original spatial resolution of the CHROMIS data, and with bandwidths in the range [3,10] Å, are retained in the data degraded to a spatial

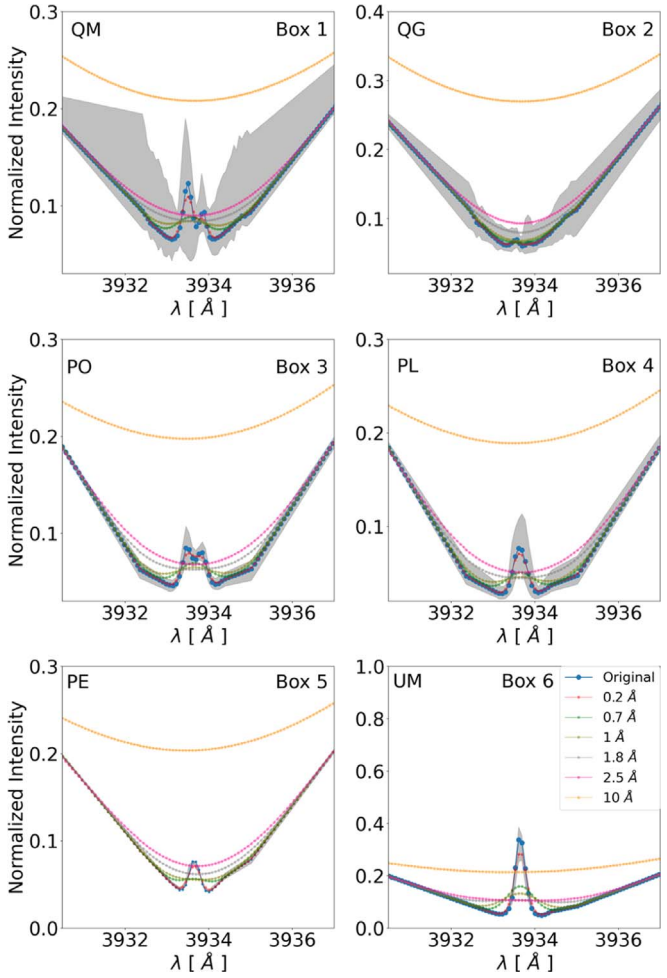

Figure 6. Ca II K line profiles derived from data averaging over the areas marked with numbers and colored boxes in Figure 2. The diverse profiles are color-coded depending on the degradation applied to the original data and according to the legend in the bottom right panel. From top to bottom we show the profiles for the selected areas in the QS (top row panels), NA (middle row panels), and SP (bottom row panels) observations, respectively. The profiles are normalized to the continuum intensity at 4000 Å (not shown). The gray shaded areas cover the range of values measured in the analyzed regions at each spectral position.

resolution up to 0.″3, while they form unresolved larger-scale bright features in the data characterized by a spatial resolution of 1″. We also note that the arc-shaped feature with largest intensity gradient seen in the original NA observations is visible in all the data derived from spatial degradation of up to 1″ and spectral bandwidths of up to 3 Å, although with lower intensity. However, in addition to this arc-shaped feature, spatial and spectral degradations bring out in the observed field several dot-like and small-scale bright structures unseen in the original data. This also applies to observations of the SP target at the Ca II K line core. In these data we notice that the appearance of the umbral and penumbral regions is only barely affected by a spatial degradation of up to 1″ and spectral degradation of up to 1 Å. Indeed, the umbral and penumbral areas are almost unaffected by the spatial degradation applied to the data, while their extension slightly decreases in the data degraded with spectral kernels larger than 1 Å.

In Appendix B we also show examples of the QS, NA, and SP regions observed at the Ca II K line core and reported in Figure 2, as returned when degraded to a spatial resolution of 4″ and to spectral bandwidths in the range [0.12,10] Å. We notice that these data show unresolved bright patterns that are rather unaffected by the spectral degradation applied to the data. We also report a marginal decrease in the umbral area for data with spectral degradation larger than 1 Å. It is worth noting that the umbral region in the degraded data shows almost the same extension to the same region in the full resolution photospheric CRISP observations and chromospheric CHROMIS data at the red wing of the Ca II K line.

3.3. Focus on Line Parameters

Figure 8 describes the impact of the spectral degradation on the K_3 and EMDX parameters derived from the diverse solar data considered in our study. In particular, we display the variation in the K_3 (left panels) and EMDX (right panels) parameters depending on the spectral kernel applied to the line profiles averaged over the whole QS region and over the QM (box 1) and QG (box 2) areas selected therein (top panels), as well as over the PO (box 3) and PL (box 4) areas in the NA region (middle panels), and the PE (box 5) and UM (box 6) areas in the SP target (bottom panels). We also report the dependence of the same parameters estimated by using the respective reference atlas data.

Figure 8 (top panels) shows that the K_3 and EMDX parameters derived from the QS and QG (QM) degraded data increase gradually for spectral bandwidths larger than 1 Å (2 Å) and are almost unaltered in observations with bandwidths in the range [0.12,1.0] Å ([0.12,2.0] Å). Therefore the sensitivity to spectral degradation of both parameters obtained from QS and QG areas is slightly different from the one derived from the QM region. We notice that the trend derived from the whole QS target reproduces the variation in the parameters derived from atlas measurements better than obtained from the other regions, except for a difference in the estimated values. The increase in the K_3 (EMDX) values is on the order of about 2%/Å (1.5%/Å) for the QS observations with spectral bandwidth larger than 1 Å.

We also studied the K_3 and EMDX parameters in the profiles derived from the PO (box 3), PL (box 4), PE (box 5), and UM (box 6) observations. As shown in Figure 8 (middle panels) the variation in the K_3 and EMDX parameters derived from the PO and PL areas are close to each other for a spectral bandwidth of about 0.2 Å and exhibit a similar behavior for all larger bandwidths, with differences that tend to decrease for bandwidths larger than 1 Å. We also note that for spectral bandwidths in the range [0.12,10] Å, the results derived from the NA region (middle panels) are rather similar to those obtained from the QM area (top panels). The same applies to the findings from the PE region (bottom panels), but limited to spectral degradations in the range [1,10] Å. In addition, Figure 8 (bottom panels) displays that for UM regions the values of the K_3 and EMDX parameters estimated from the spectrally degraded data increase gradually for bandwidths larger than about 3 Å, while the values of both parameters decrease in observations with a spectral degradation in the range [0.12,2] Å. This decrease in the values of the K_3 and EMDX parameters is on the order of 35%/Å and 18%/Å, respectively, while the increase in the parameters for the data with bandwidths in the range [3, 10] Å is on the order of 1%/Å. Similarly to results from the QS and QG regions, the parameters computed for the PE area are almost unaltered in observations with spectral bandwidth in the range [0.2, 1.0] Å,

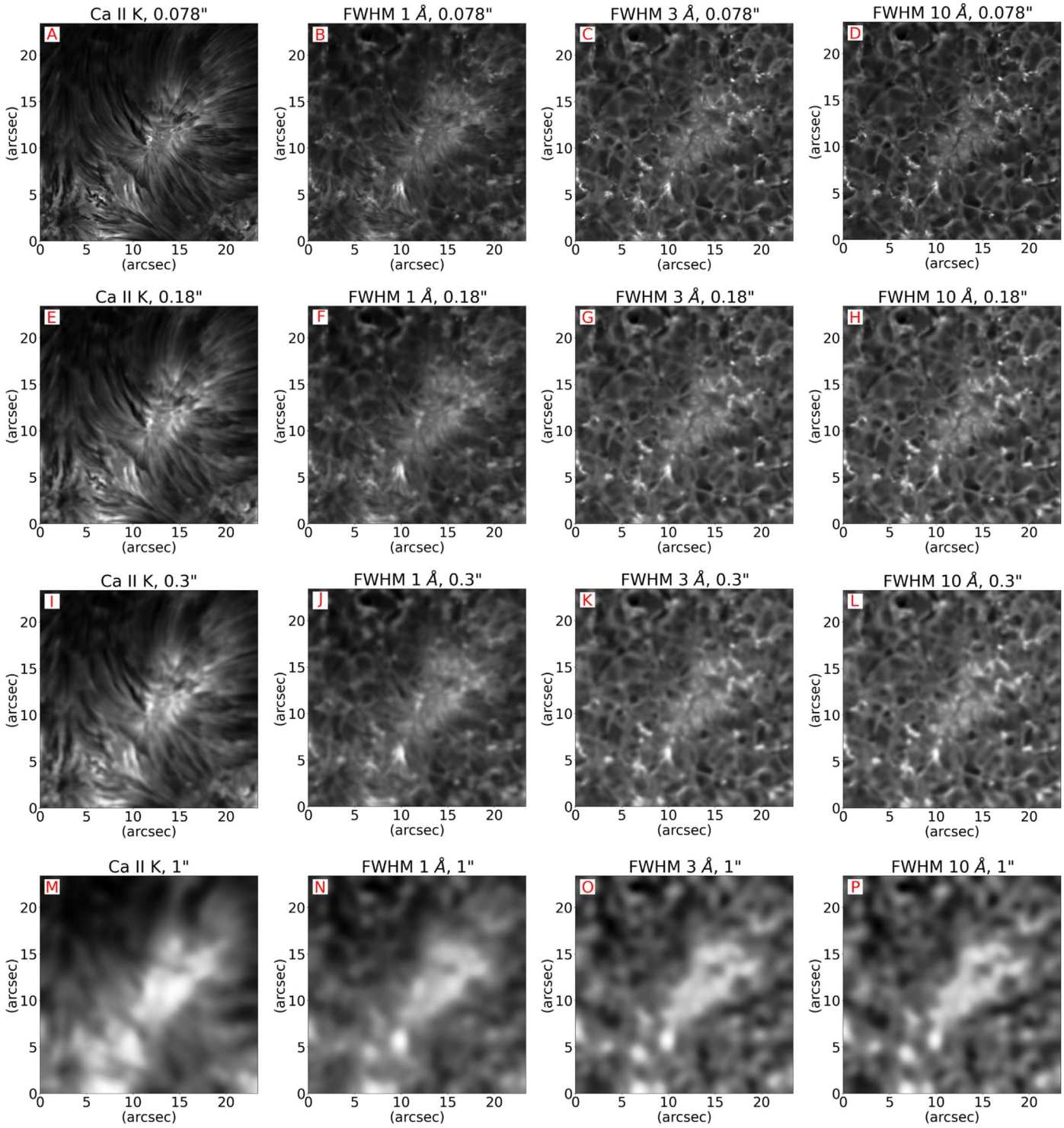

Figure 7. Examples of the original (panel (A)) and degraded (all other panels) images at the Ca II K line core of the QS region, to account for the diverse bandwidths and spatial resolutions of the most prominent series of available Ca II K observations. Each row shows examples of data characterized by a given pixel scale and by different bandwidths. From top to bottom, we show data at the original pixel scale of the CHROMIS observations (panels (A)–(D)) and degraded to a spatial resolution of $0\farcs18$ (panels (E)–(H)), $0\farcs3$ (panels (I)–(L)), and $1\farcs0$ (panels (M)–(P)), as is in the case of the SUNRISE/IMaX, Hinode/SOT, and SDO/HMI observations, respectively. For each of these observations, from left to right we show the data at the spectral resolution of the CHROMIS observations of 0.12 Å, and spectrally degraded with Gaussian kernels with a FWHM of 1, 3, and 10 Å. Each image is shown using the intensity interval that enhances the visibility of the solar features therein.

while they increase gradually by about 1%/Å for the data with bandwidths in the range [1,10] Å.

We notice that the K_3 and EMDX parameters computed on each observed region vary with the spectral degradation applied to the data in a rather similar way. Therefore, in the following we further consider the characteristics of the K_3 variation only.

We report that the best relation describing the changes in the K_3 parameter on the spectral bandwidth of the data is a

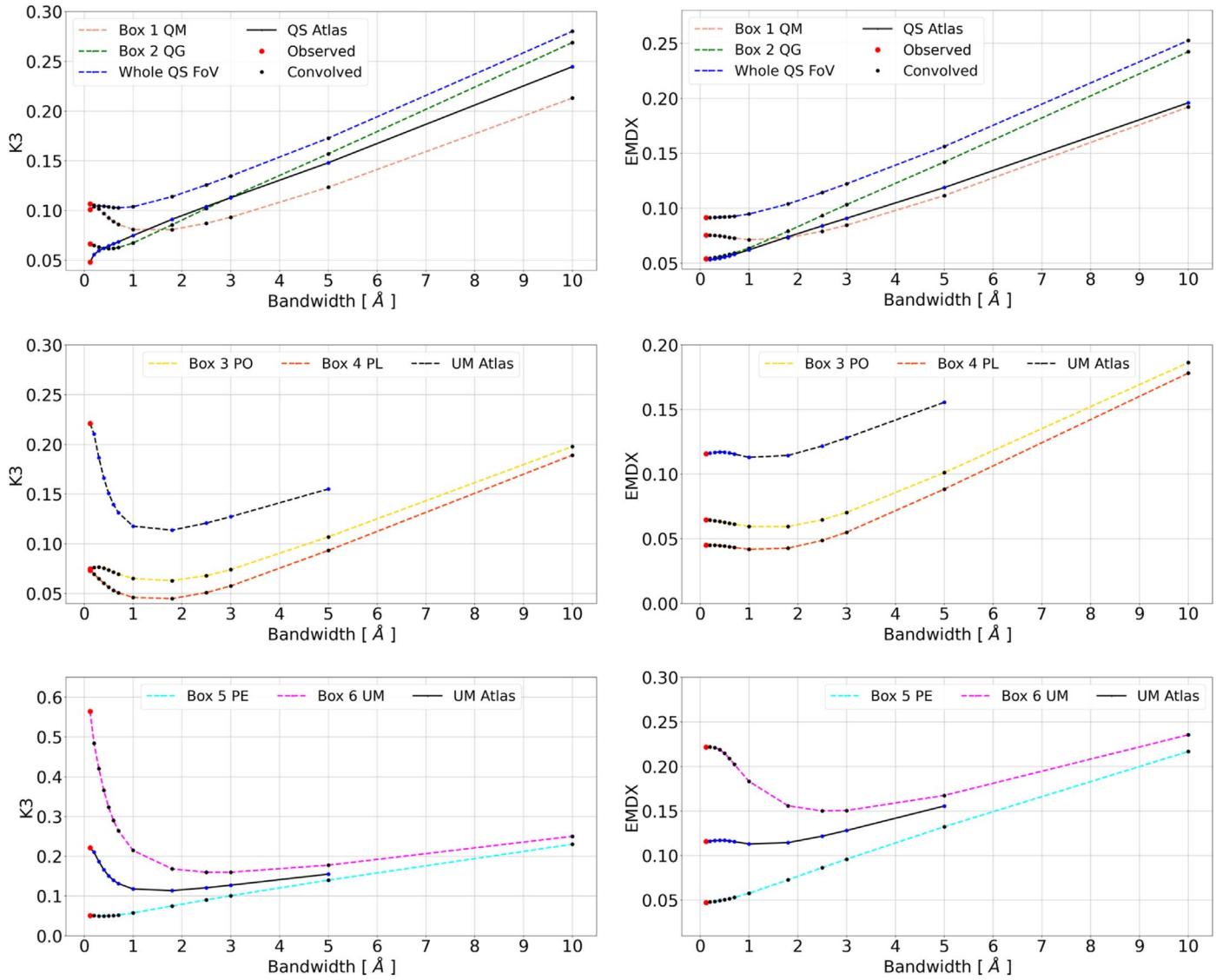

Figure 8. Dependence of the K_3 (left-column panels) and EMDX (right-column panels) parameters estimated from the Ca II K line measurements on the QS region and on the QM and QG areas therein (top row panels), PO and PL areas in the NA target (middle row panels), and PE and UM areas selected in the SP observation (bottom row panel), depending on the spectral degradation applied to the analyzed data. Overplotted to each panel is the variation in the parameter derived from the relevant atlas data (black solid line) after their spectral degradation with the various kernels used in our study. Find information about the atlas data in Section 2.2.

Table 1
Results from K_3 Parameter Fitting

Region	a [10^{-5}]	b [10^{-4}]	c [10^{-3}]	d [10^{-2}]	e [10^{-2}]	f [10^{-1}]	Mean SD [10^{-4}]
QM	-3.5 ± 2.5	8.8 ± 4.9	-8.1 ± 2.9	3.5 ± 0.7	-6.2 ± 0.6	1.1 ± 0.01	6.8
QG	-9.5 ± 0.76	19 ± 1.4	-14 ± 0.8	4.3 ± 0.2	-3.4 ± 0.2	0.7 ± 0.004	2.0
QS	-2.4 ± 2.9	-4 ± 5.5	1.5 ± 3.3	2.8 ± 0.7	-0.2 ± 0.7	1 ± 0.02	8.1
PE	-7.2 ± 0.7	15 ± 1.3	-10 ± 0.8	3.1 ± 0.2	-1.8 ± 0.2	0.5 ± 0.004	1.8
UM	-141 ± 22	294 ± 42	-209 ± 25	65 ± 5.8	-92 ± 5	6.5 ± 0.1	61.5
QS Atlas	5.7 ± 3.5	-11 ± 6.5	7.8 ± 3.9	-2.2 ± 0.9	4.6 ± 0.8	4.6 ± 0.2	9.2
UM Atlas	-136 ± 80	191.4 ± 86.7	-102.9 ± 31.7	26.7 ± 4.8	-32.7 ± 2.8	2.6 ± 0.05	15.4

Note. Columns are: solar region over which the relationship was studied, best-fit parameters (a, b, c, d, e, f) with their 1σ uncertainties, and the mean standard deviation (SD) between original and curves of the fits. Find more details in Sections 2.2 and 3.3.

polynomial function of the fifth order that is represented by the equation

$$K_3 = ax^5 + bx^4 + cx^3 + dx^2 + ex + f, \quad (1)$$

where x is the spectral bandwidth considered, expressed in Å. Table 1 summarizes the $a-f$ parameters for the various studied data.

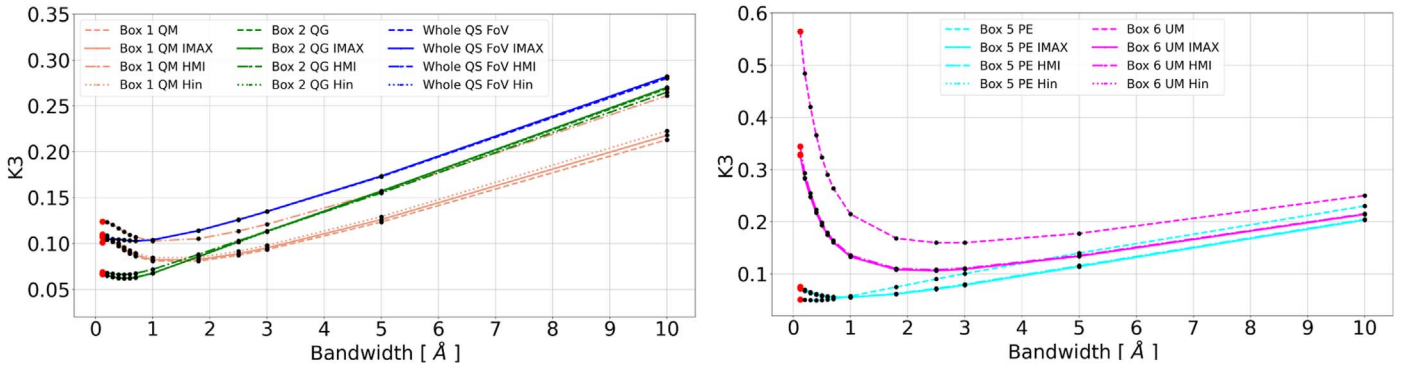

Figure 9. Dependence of the K_3 parameter estimated from the Ca II K line measurements on the QS, QG, and QM areas (top panel) and on the PE and UM regions (bottom panel), depending on the spectral and spatial degradation applied to the analyzed data, representative of various observations. Find more details in Sections 3.2 and 3.3.

We find that the fitted curves follow the data derived from the observations with minute deviations. Indeed, all the fits give mean standard deviations between the original and fitted curves in the range $[1.8,15.4]\times10^{-4}$, except for the UM data, which show a mean deviation of about 62×10^{-4}. However, we notice that the fitting of the UM data is slightly better represented by a polynomial function of the sixth order,[9] which results in an average deviation of about 26×10^{-4}. Note that we derived the mean deviation from the average difference between original and fitted values, and the 1σ uncertainty from the diagonal values of the covariance matrix of the optimal coefficients computed with the *scipy.optimize.curve _fit* function in the *Python* language.

We then considered the effect of the spatial degradation on the values of the K_3 parameter estimated for the various solar regions and spectral bandwidths considered in our study.

Figure 9 displays the variation in the K_3 parameter derived from the line profiles averaged over the whole QS region and selected QM and QG areas (top panel) therein, as well as over the PE and UM regions (bottom panel) of the SP target, by considering the CHROMIS data and those obtained from the various spectral and spatial kernels applied to them. Similarly to findings in Figure 8, results from the PL and PO areas are close to the ones reported for the QM and UM regions, respectively, and are thus not shown.

Results in Figure 9 suggest that the effect of the spatial degradation on K_3 vales depends on the solar target. It is significant for the selected areas representative of the QM region (box 1) in the QS target, and of the PE (box 5) and UM (box 6) areas in the SP region. In particular, for observations of the QM, PE, and UM regions, K_3 changes of about [2,30]%, $-$[5, 20]%, and $-$[15,40]% maximum when the data are degraded to observations with spatial resolution from $0\farcs18$ to $1''$, which represent the cases of the SUNRISE/IMaX and SDO/HMI observations, respectively. K_3 changes in QM, PE, and UM areas from about 5%/Å to 20%/Å, 15%/Å to 30%/Å, 0.1%/Å to 30%/Å minimum to maximum when considering data with a spectral degradation given by bandwidths in the range [2,10] Å. For the QG and QS areas the spatial degradation affects only minutely the estimated value of the K_3 parameter.

[9] Described by the equation $K_3 = ax^6 + bx^5 + cx^4 + dx^3 + ex^2 + fx + g$, with the following coefficients: $a = (0.8\pm0.2)10^{-5}$, $b = (-0.02\pm0.3)10^{-4}$, $c = (0.01\pm0.2)10^{-3}$, $d = (-0.5\pm7)10^{-2}$, $e = (0.01\pm0.0009)10^{-2}$, $f = (-0.1\pm0.05)10^{-1}$, $g = (6.8\pm0.0008)10^{-1}$.

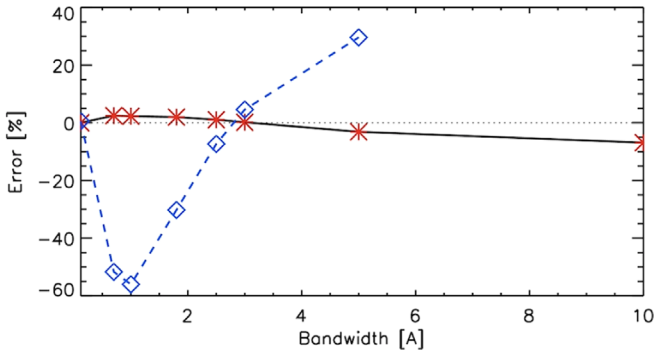

Figure 10. Error [%] in the K_3 values estimated from atlas data representative of QS region (solid black line, red star symbols), and NA and SP (dashed blue line, diamond blue symbols) regions, depending on the spectral degradation applied to the data. For the sake of clarity overplotted is the null error line (dotted line).

4. Discussion

The observations analyzed in our study were compensated for residual effects of atmospheric turbulence, and calibrated with atlas measurements before their degradation to match the diverse spectral and spatial resolutions considered. However, they are not compensated for stray-light contamination, which is estimated to be low and to mostly come from the SST instruments (Scharmer et al. 2019). Intensity values analyzed in our study may thus suffer from incomplete compensation for stray light, because the spectral intensity calibration applied to the data using the disk-center atlas spectrum as reference does not remove all instrumental effects. Based on comparison between intensity values measured in the QS target and in the atlas reference we expect compensation for stray light to affect the line core intensities reported from our study with an increase in their values of about 40% and 80% in QS and PO penumbral data, respectively. Moreover, we would like to emphasize that the observations and line intensities reported in this study might not be representative of all the similar solar and stellar data. Indeed, we highlight that they refer to the specific level of solar magnetism and solar activity framed by the observations analyzed in our study.

In addition, we have reported results based on line profile data that combine measured values in the inner part of the line and extrapolated values in the line wings. As stated above, these data simulate low-resolution spectral observations in the

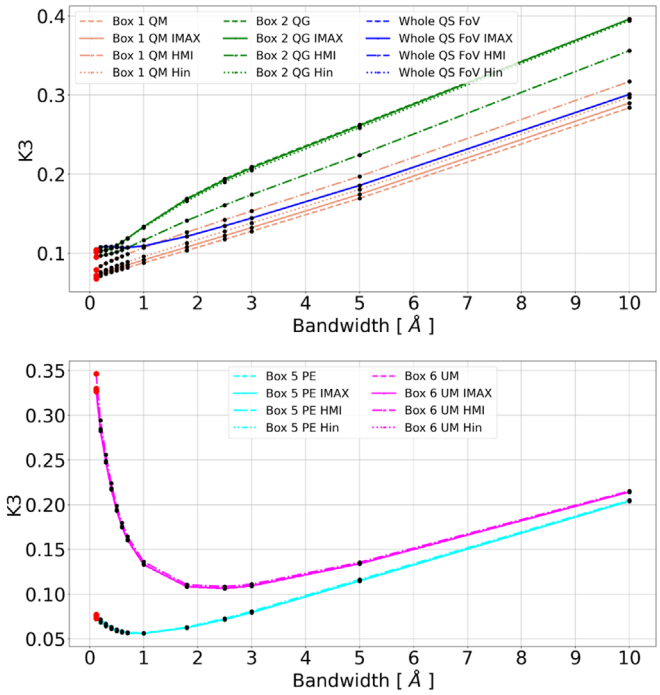

Figure 11. Dependence of the K_3 parameter estimated from the Ca II K line measurements on the QS, QG, and QM areas (top panel) and on the PE and UM regions (bottom panel), depending on the spectral and spatial degradation applied to the analyzed data, representative of various observations. Here the reported values derive from average Ca II K line profiles computed pixelwise on spectrally and spatially degraded data. Find more details in Section 4.

line wings and high-resolution observations in the line core. In addition, the extrapolated values do not account for the many lines that populate the spectra adjacent to the Ca II K line core. We investigated the impact of the unaccounted line blending in the obtained results. To this end, we analyzed atlas data and applied to these all the processing steps performed on the observations analyzed in our study.

Figure 10 summarizes information about the error expected for our estimated values by missing the effect of line blending in the analyzed data. We notice that this error can lead to either underestimating or overestimating the K_3 values depending on the observed region and bandwidth of the analyzed data. In particular, for the QS and PL data, it leads to underestimating the K_3 parameter up to 2.5% for data with 0.7 Å bandwidth, while there is an overestimation of the values for the data with a spectral degradation in the rage [3,10] Å. In this case the error increases linearly up to about 7%. On the other hand, for the PO and UM data represented by the corresponding atlas, the approximation applied in our study can lead to an overestimation of K_3 values up to 50% for data with a bandwidth of 1 Å, and to an underestimation of the values for data with spectral widths in the range [3,5] Å. In this case the underestimation error increases linearly up to about 30%. Note that the smaller range of bandwidths over which we can investigate the effect of line blending in the UM atlas data derives from the fact that those measurements are available only for wavelengths larger than 3920.5 Å. Overall, the estimated errors suggest that the findings presented above shall be deemed to be indicative of the studied dependence and as an underestimation of its effects.

Furthermore, we have presented results from spatially resolved data, both observations and line profiles, as well as from average profiles computed over small areas (20×20 pixels wide, i.e., covering a photospheric region of about $0\farcs8 \times 0\farcs8$) selected to represent six solar features in the ambient to which they belong. We note that the latter data describe observations that are indeed characterized by a lower spatial resolution than that of the original CHROMIS measurements. This can explain the small dependence on the explored spatial degradations of most of the K_3 values reported in Figure 9. We however acknowledge that those results may not represent findings from similar estimations based on different computational approaches to account for the data characteristics. In particular, we found that the dependence of K_3 values on the spectral and spatial degradation of the data slightly differ whether K_3 is estimated by maintaining the original resolution of the observations or by degrading it to the one of the selected small areas. The impact of the approach applied to estimate K_3 is however minute. In particular, Figure 11 shows the variation in the K_3 parameter derived from data of the QS, QM, and QG regions (top panel), and of the PE and UM areas (bottom panel), by considering the original CHROMIS observations and the data obtained from the spectral and spatial kernels applied pixelwise to them. The results in Figure 11 suggest that the diverse approaches, namely, considering the average profile of small areas or profiles derived pixelwise, affect the K_3 values obtained, but they only marginally impact the exact form of the relation describing the K_3 variation on data characteristics. Indeed, for the ranges of spectral and spatial degradations explored in our study, we found that this relationship is basically linear over the range [2,10] Å for all the investigated regions.

Finally, in our study we considered K_3 to quantify the Ca II K brightening in the diverse image pixels and solar features in our data sets, but this quantity is also defined in the literature as the line core intensity contrast C, where $C = I/I_{\rm QS}$, and I and I_{QS} are the Stokes-I intensities at the Ca II K line core over each image pixel and mean QS intensity averaged over the entire FoV analyzed, respectively; see, e.g., Kahil et al. (2017).

In Figure 12 we show the variation in the line core intensity contrast estimated on the whole QS region and on the several selected areas of Figure 2. First, we notice that the values and trends in Figure 12 largely differ from the ones reported in Figure 8 due to the diverse reference intensities employed to derive the quantities in the respective figures. Besides, Figure 12 displays that the line core contrast decreases monotonically with the increase in the spectral degradation of the data for observations of the whole QS target and UM areas, while it shows a different variation on the selected areas of QS (QM box 1 and QG box 2) and of PE (box 5) regions. The decrease in the line core contrast in average QS and UM regions is particularly severe for bandwidths up to about 2.5 Å and on the order of 40%/Å and 500%/Å, respectively. The results from the selected QS area characterized by regular granulation (QG box 2) display a hook-like trend with the decrease in the estimated contrast up to a minimum for bandwidths up to about 1 Å and increase in the contrast for larger spectral widths. On the other hand, the contrast values derived from the PE area show a monotonic increase with the bandwidth, which is on the order of 50%/Å for observations with bandwidth up to about 5 Å.

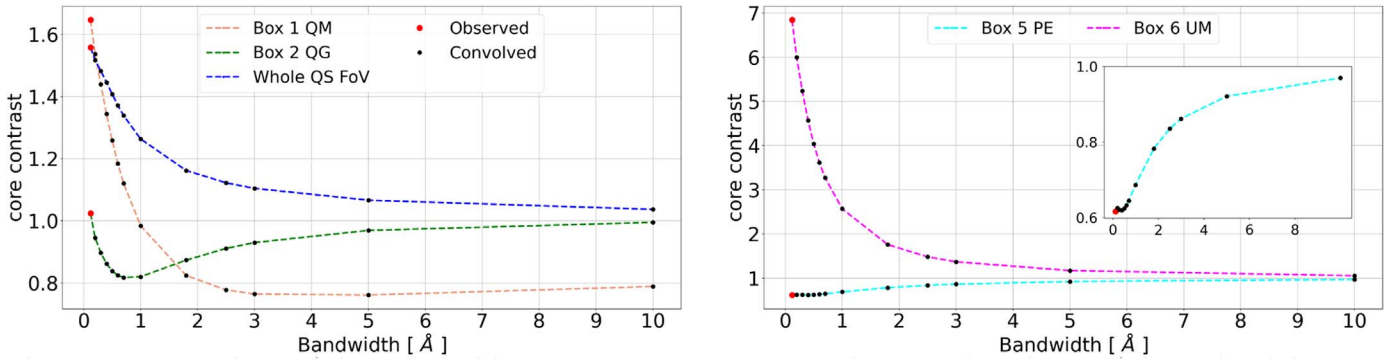

Figure 12. Dependence of the estimated line core intensity contrast on the spectral resolution of the analyzed data, on the whole QS region and on the QM and QG areas therein (left panel), as well as on the PE and UM areas selected in the SP observations (right panel). See Section 4 for more details.

5. Summary and Conclusions

We investigated the variation in the observations and line profile measurements at the Ca II K line depending on the spectral bandwidth and spatial resolution of the data, and on the ambient in the solar atmosphere. We used state-of-the-art observations of the solar photosphere and chromosphere obtained with the CRISP spectropolarimeter and CHROMIS spectrometer operating at the Swedish Solar Telescope. We studied three data sets that relate to very different conditions in the solar atmosphere, representative of a quiet-Sun area, a region with plages and several small pores, and a large sunspot with umbra and penumbra.

First, we noticed the large heterogeneity that characterizes the Ca II K line profiles measured over the studied regions when considered at the full spectral and spatial resolution of the CHROMIS data. This heterogeneity is particularly evident in the data derived from the QS areas, which show intensity variations due to, e.g., *p*-modes oscillations. However, different and distinguishable elements of the Ca II K line profiles derived from the diverse studied regions are retained when the data are averaged over areas selected to represent the solar region to which they belong.

We then noticed that the effect of spectral degradation on Ca II K observations and line profiles depends on both the bandwidth employed and observed solar region. As expected, smearing the original data with a spectral kernel leads to greater mixing of photospheric and chromospheric emissions that strongly affects the appearance of the observed regions. In particular, degrading the observations with larger kernels leads to the appearance of smaller-scale structures and finer details. We found that, among the three regions considered in our study, the one with plages and several small pores shows the largest change in its appearance with the various spectral degradation kernels applied. Moreover, we noticed that the spatial degradation impacts the data derived from larger bandwidths more than those obtained with smaller ones. However, the spatial degradation barely affects the appearance of the solar region observed with bandwidths up to 1 Å, as well as for those observed with a spectral bandwidth in the range [3,10] Å.

Finally, we noticed that the K_3 and EMDX parameters employed for the monitoring of the solar and stellar chromospheric activity vary with the spectral bandwidth as described by a fifth-order polynomial function for all the observed solar regions. From the best-fitting functions of the data we derived parameters that can be used to intercalibrate results from Ca II K line observations taken with different instruments in diverse regions of the solar atmosphere.

We would like to emphasize that the line intensities reported from our study refer to the specific level of solar magnetism and solar activity framed by the analyzed observations. Besides, we note that the analyzed data are not representative of all the QS, plages, and sunspot regions of the Sun and other stars. Indeed, regions that appear rather similar at the stellar surface may be characterized by a completely different plasma and magnetic topology at higher atmospheric heights due to, e.g., the presence of strong field concentrations in the vicinity of the analyzed region and affecting it. On the other hand, we note that starting from their common doubly reversed profile, the Ca II H and K lines share many properties being formed in the chromosphere under similar conditions. We thus expect that the findings from our study on the dependence of the Ca II K observations and line profiles on characteristics of the data and observed solar ambient can also qualitatively apply to Ca II H line data.

The authors thank Vincenzo Andretta for useful comments. This study was partly supported by the European Union's Horizon 2020 research and innovation program under grant agreements No. 739500 (PRE-EST project) and No. 824135 (SOLARNET project), the Italian MIUR-PRIN grant 2017APKP7T on "Circumterrestrial Environment: Impact of Sun-Earth Interaction," and the Italian agreement ASI-INAF 2021-12-HH.0 "Missione Solar-C EUVST—Supporto scientifico di Fase B/C/D."

The Swedish 1 m Solar Telescope is operated on the island of La Palma by the Institute for Solar Physics of Stockholm University in the Spanish Observatorio del Roque de los Muchachos of the Instituto de Astrofísica de Canarias.

This research is supported by the Research Council of Norway, project number 325491 and through its Centers of Excellence scheme, project No. 262622.

This study has made use of SAO/NASA Astrophysics Data System's bibliographic services.

Appendix A
Examples of Line Profiles

Figure 13 shows examples of line profiles derived from other areas representative of QM and QG features selected nearby the ones reported in Figure 2. See Section 3 for more details.

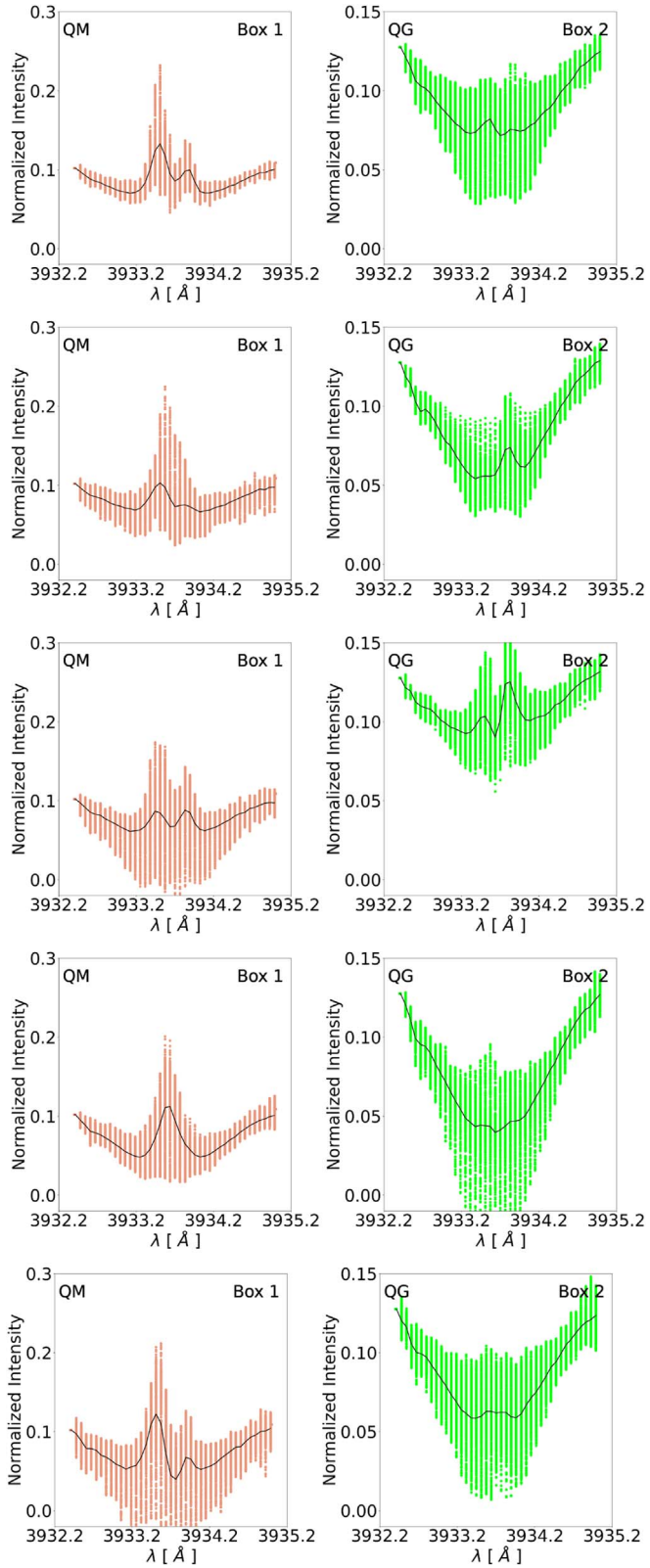

Figure 13. Examples of Ca II K line profiles analyzed in our study. These were obtained from 20 × 20 pixels wide areas overlapping the QM and QG boxes marked with numbers 1 and 2 in Figure 2 or similar adjacent areas. From top to bottom, the panels in each row show results derived from boxes marked in Figure 2, and from the boxes adjacent to these in their uppermost, lowermost, leftward, and rightward sides, representative of the QM (left-column panels) and QG (right-column panels) regions. Black solid lines show the mean profiles derived from the spatially resolved data available at each observed spectral position.

Appendix B
Examples of Spectrally and Spatially Degraded Data

Figure 14 shows examples of original and degraded data for the QS region observed in the red wing of the Ca II K line at +1.05 Å from the line core. Figures 15 and 16 display examples of original and degraded data for the NA observations that include plages and pores, and SP observations with umbral and penumbral regions, respectively. Figure 17 shows examples of CHROMIS

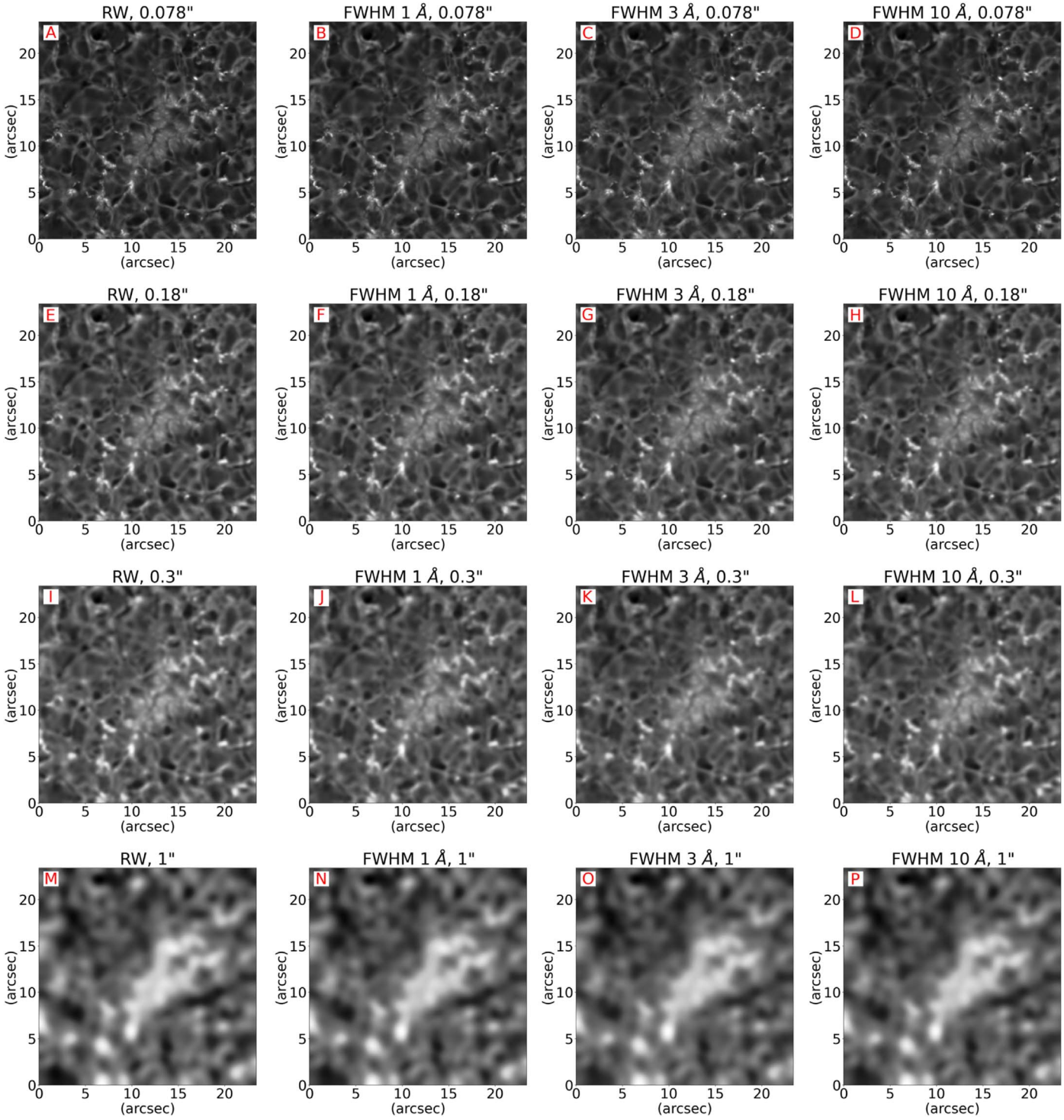

Figure 14. Examples of the original (panel (A)) and degraded (all other panels) images of the QS region observed in the red wing (RW) at +1.05 Å from the Ca II K line core, to account for the diverse bandwidths and spatial resolutions of the most prominent series of available Ca II K observations. Each row shows examples of data characterized by a given pixel scale and by different bandwidths. From top to bottom, we show data at the original pixel scale of the CHROMIS observations (panels (A)–(D)) and degraded to a spatial resolution of 0.″18 (panels (E)–(H)), 0.″3 (panels (I)–(L)), and 1.″0 (panels (M)–(P)), as is in the case of the SUNRISE/IMaX, Hinode/SOT, and SDO/HMI observations, respectively. For each of these observations, from left to right we show the data at the spectral resolution of the CHROMIS observations of 0.12 Å, and the data spectrally degraded with Gaussian kernels with a FWHM of 1, 3, and 10 Å. Each image is shown using the intensity interval that enhances the visibility of the solar features therein.

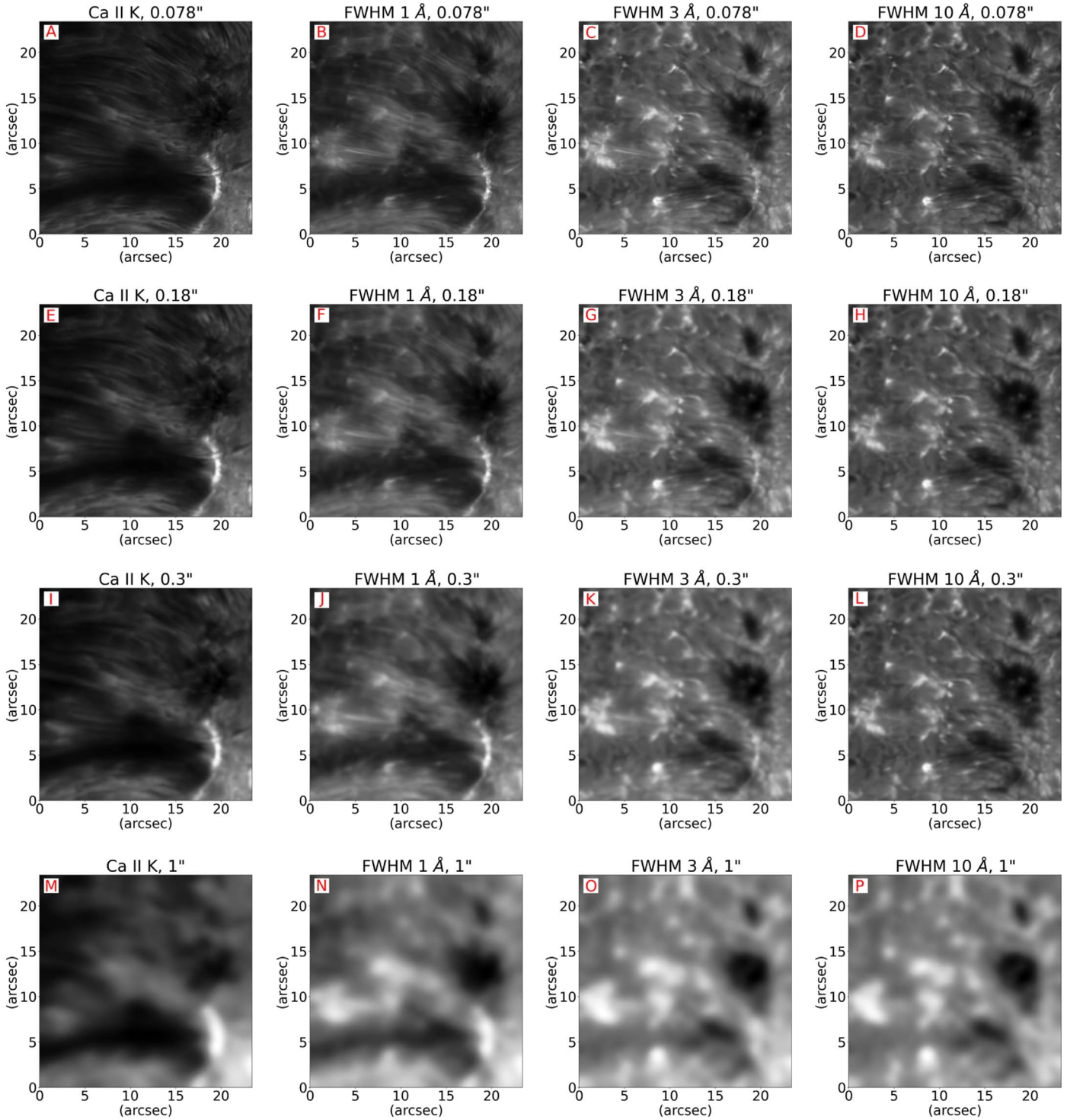

Figure 15. Examples of the original (panel (A)) and degraded (all other panels) images at the Ca II K line core of the NA region including areas with plages (PL) and pores (PO), to account for the diverse bandwidths and spatial resolutions of the most prominent series of available Ca II K observations. Each row shows examples of data characterized by a given pixel scale and by different bandwidths. From top to bottom, we show data at the original pixel scale of the CHROMIS observations (panels (A)–(D)) and degraded to a spatial resolution of $0\farcs18$ (panels (E)–(H)), $0\farcs3$ (panels (I)–(L)), and $1\farcs0$ (panels (M)–(P)), as is in the case of the SUNRISE/IMaX, Hinode/SOT, and SDO/HMI observations, respectively. For each of these observations, from left to right we show the data at the spectral resolution of the CHROMIS observations of 0.12 Å, and the data spectrally degraded with Gaussian kernels with a FWHM of 1, 3, and 10 Å. Each image is shown using the intensity interval that enhances the visibility of the solar features therein.

observations in the Ca II K line core degraded to the moderate spatial resolution of $4''$ and spectral degradation given by bandwidths in the range [0.12,10] Å, as for the characteristics of most of the existing series of full-disk synoptic solar observations at the Ca II K line. See Section 3.2 for more details.

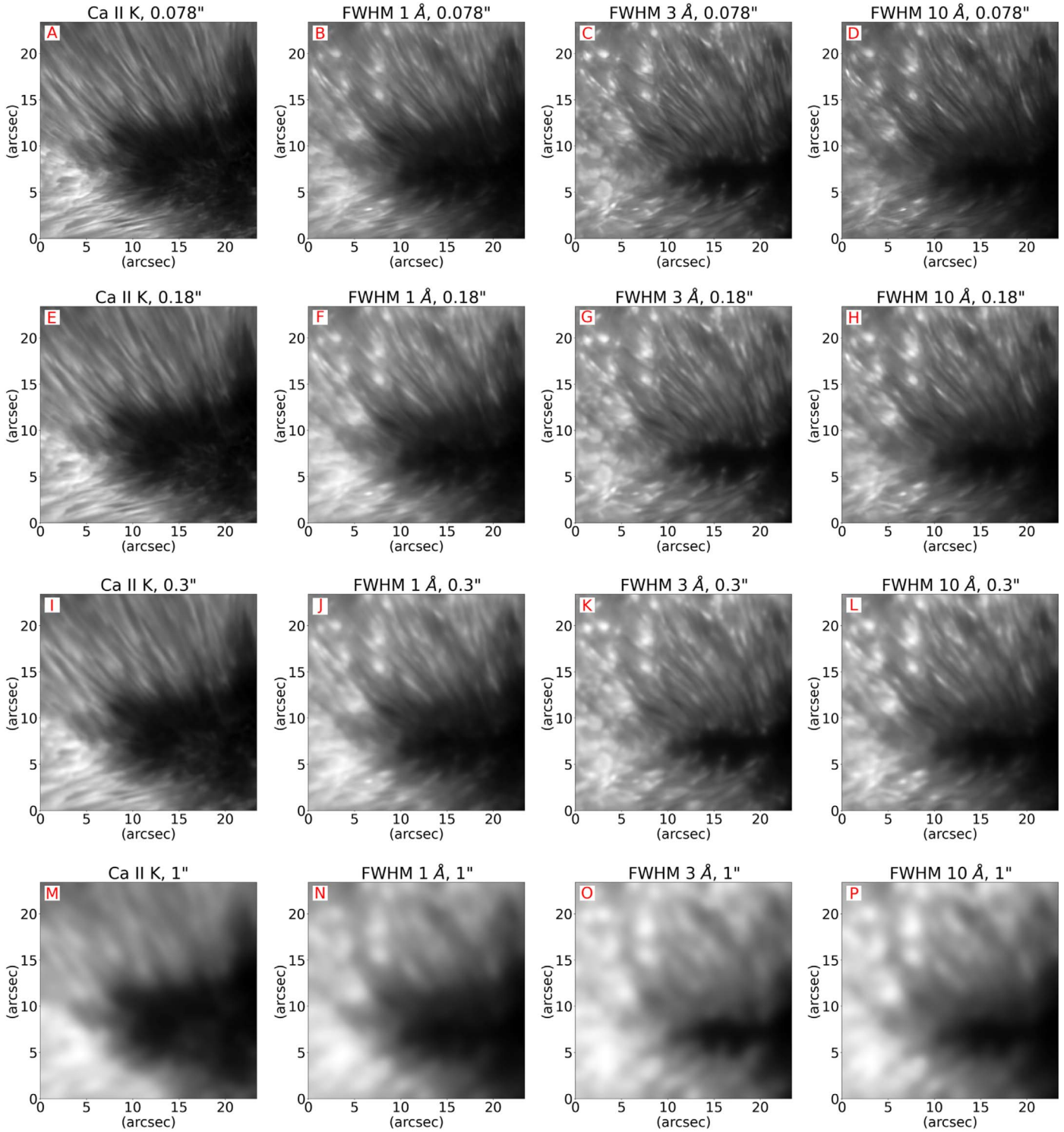

Figure 16. Examples of the original (panel (A)) and degraded (all other panels) images at the Ca II K line core of the SP region with UM and PE areas, to account for the diverse bandwidths and spatial resolutions of the most prominent series of available Ca II K observations. Each row shows examples of data characterized by a given pixel scale and by different bandwidths. From top to bottom, we show data at the original pixel scale of the CHROMIS observations (panels (A)–(D)) and degraded to a spatial resolution of $0\farcs18$ (panels (E)–(H)), $0\farcs3$ (panels (I)–(L)), and $1\farcs0$ (panels (M)–(P)), as is in the case of the pixel scale of the SUNRISE/IMaX, Hinode/SOT, and SDO/HMI observations, respectively. For each of these observations, from left to right we show the data at the spectral resolution of the CHROMIS observations of 0.12 Å, and the data spectrally degraded with Gaussian kernels with a FWHM of 1, 3, and 10 Å. Each image is shown using the intensity interval that enhances the visibility of the solar features therein.

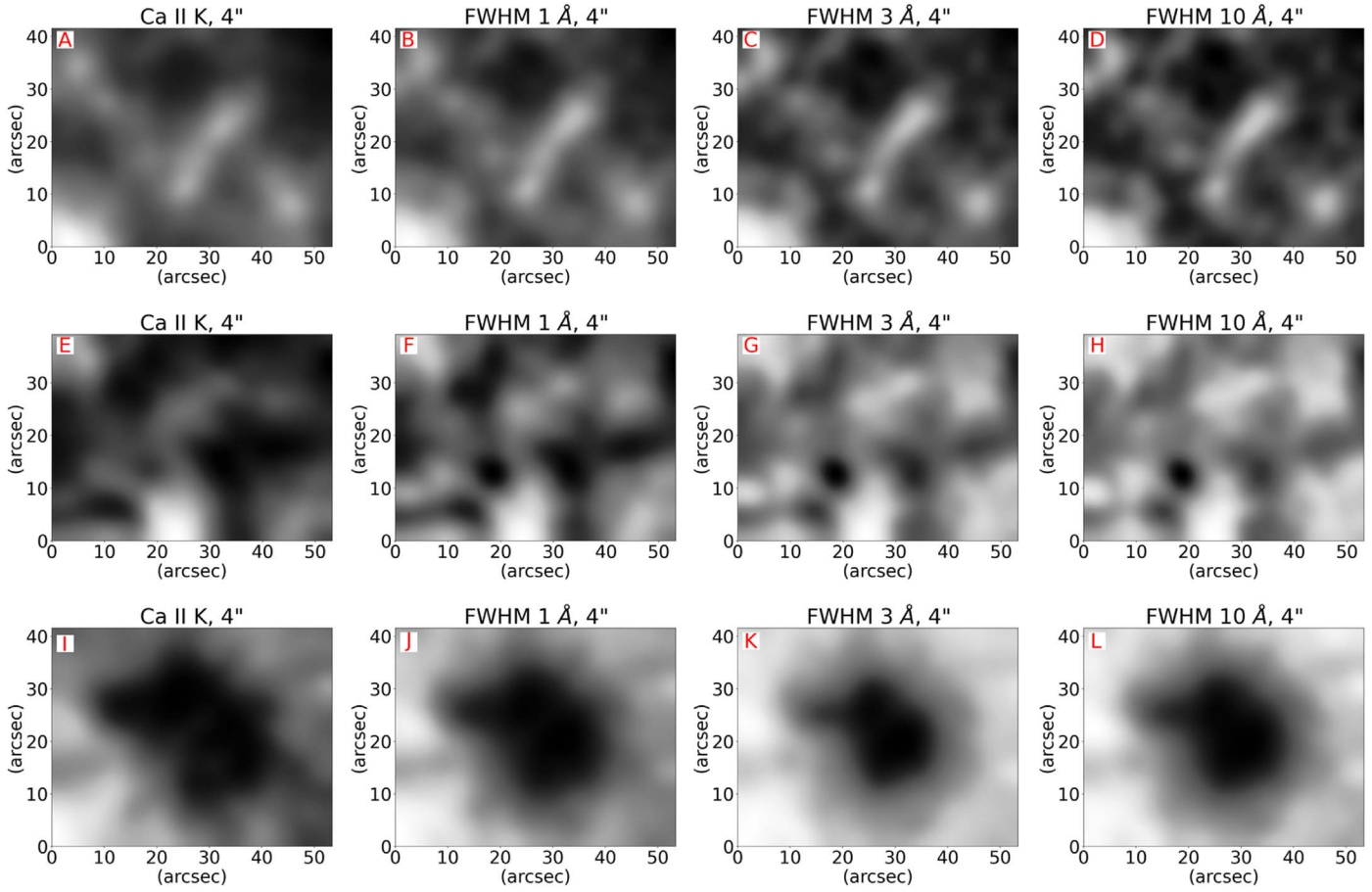

Figure 17. Examples of Ca II K images in the line core degraded to the moderate spatial resolution of 4″, which meets the characteristics of several existing series of synoptic full-disk solar observations at the Ca II K line, of a quiet-Sun area (top row panels), an active region with plages and several pores (middle row panels), and a sunspot with umbra and penumbra (bottom row panels). From left to right, the panels in each row show the three regions as observed at the original spectral resolution of the CHROMIS data (0.12 Å, panels (A), (E), (I)), and with bandwidths of 1 Å (panels (B), (F), (J)), 3 Å (panels (C), (G), (K)), and 10 Å (panels (D), (H), (L)). Each image is shown using the intensity interval that enhances the visibility of the solar features therein.

ORCID iDs

M. Murabito https://orcid.org/0000-0002-0144-2252
I. Ermolli https://orcid.org/0000-0003-2596-9523
T. Chatzistergos https://orcid.org/0000-0002-0335-9831
S. Jafarzadeh https://orcid.org/0000-0002-7711-5397
F. Giorgi https://orcid.org/0000-0002-0974-2401
L. Rouppe van der Voort https://orcid.org/0000-0003-2088-028X

References

Auvergne, M., Bodin, P., Boisnard, L., et al. 2009, A&A, 506, 411
Babcock, H. W., & Babcock, H. D. 1955, Natur, 175, 296
Baliunas, S. L. 1984, in Future of Ultraviolet Astronomy Based on Six Years of IUE Research, ed. J. M. Mead, R. D. Chapman, & Y. Kondo (Washington, D.C.: NASA), 64
Baliunas, S. L., Donahue, R. A., Soon, W. H., et al. 1995, ApJ, 438, 269
Barthol, P., Gandorfer, A., Solanki, S. K., et al. 2011, SoPh, 268, 1
Bjørgen, J. P., Sukhorukov, A. V., Leenaarts, J., et al. 2018, A&A, 611, A62
Borucki, W. J., Koch, D., Basri, G., et al. 2010, Sci, 327, 977
Bose, S., Henriques, V. M. J., Joshi, J., & Rouppe van der Voort, L. 2019, A&A, 631, L5
Chatzistergos, T., Ermolli, I., Krivova, N. A., et al. 2020, A&A, 639, A88
Chatzistergos, T., Ermolli, I., Krivova, N. A., et al. 2022a, A&A, 667, A167
Chatzistergos, T., Ermolli, I., Krivova, N. A., & Solanki, S. K. 2019a, A&A, 625, A69
Chatzistergos, T., Ermolli, I., Solanki, S. K., & Krivova, N. A. 2018, A&A, 609, A92
Chatzistergos, T., Ermolli, I., Solanki, S. K., et al. 2019b, A&A, 626, A114
Chatzistergos, T., Ermolli, I., Solanki, S. K., et al. 2019c, SoPh, 294, 145
Chatzistergos, T., Krivova, N. A., Ermolli, I., et al. 2021, A&A, 656, A104
Chatzistergos, T., Krivova, N. A., & Ermolli, I. 2022b, FrASS, 9, 336
de la Cruz Rodríguez, J., Löfdahl, M. G., Sütterlin, P., Hillberg, T., & Rouppe van der Voort, L. 2015, A&A, 573, A40
Delbouille, L., Roland, G., & Neven, L. 1973, Atlas photométrique du spectre solaire de λ 3000 á λ 10000 (Liége: Université de Liége, Institut d'Astrophysique)
Dineva, E., Pearson, J., Ilyin, I., et al. 2022, AN, 343, e223996
Duncan, D. K., Vaughan, A. H., Wilson, O. C., et al. 1991, ApJS, 76, 383
Eberhard, G., & Schwarzschild, K. 1913, ApJ, 38, 292
Engvold, O., Vial, J.-C., & Skumanich, A. 2019, The Sun as a Guide to Stellar Physics (Amsterdam: Elsevier)
Ermolli, I., Giorgi, F., & Chatzistergos, T. 2022, FrASS, 9, 352
Esteban Pozuelo, S., de la Cruz Rodríguez, J., Drews, A., et al. 2019, ApJ, 870, 88
Gondoin, P., Gandolfi, D., Fridlund, M., et al. 2012, A&A, 548, A15
Hale, G. E., & Ellerman, F. 1903, PYerO, 3, I.1
Hall, J. C., Lockwood, G. W., & Gibb, E. L. 1995, ApJ, 442, 778
Hall, J. C., Lockwood, G. W., & Skiff, B. A. 2007, AJ, 133, 862
Howard, R. 1959, ApJ, 130, 193
Ichimoto, K., Lites, B., Elmore, D., et al. 2008, SoPh, 249, 233
Kahil, F., Riethmüller, T. L., & Solanki, S. K. 2017, ApJS, 229, 12
Keil, S. L., & Worden, S. P. 1984, ApJ, 276, 766
Koch, D. G., Borucki, W. J., Basri, G., et al. 2010, ApJL, 713, L79
Lefebvre, S., Ulrich, R. K., Webster, L. S., et al. 2005, MmSAI, 76, 862

Leighton, R. B. 1959, ApJ, 130, 366
Leighton, R. B. 1960, in IAU Symp. 12, Aerodynamic Phenomena in Stellar Atmospheres, ed. R. N. Thomas (Cambridge: Cambridge Univ. Press), 321
Linsky, J. L. 1968, PhD thesis, Harvard Univ.
Linsky, J. L. 1970, SoPh, 11, 355
Linsky, J. L. 2017, ARA&A, 55, 159
Linsky, J. L., & Avrett, E. H. 1970, PASP, 82, 169
Lites, B. W., Scharmer, G. B., Berger, T. E., & Title, A. M. 2004, SoPh, 221, 65
Löfdahl, M. G. 2002, Proc. SPIE, 4792, 146
Löfdahl, M. G., Hillberg, T., de la Cruz Rodríguez, J., et al. 2021, A&A, 653, A68
Lourenço, A., Carvalho, S., Barata, T., et al. 2019, OAst, 28, 165
Maldonado, J., Phillips, D. F., Dumusque, X., et al. 2019, A&A, 627, A118
Malherbe, J.-M., Bualé, I., Crussaire, D., Cornu, F., & Corbard, T. 2022, AdSpR,
Martínez Pillet, V., Del Toro Iniesta, J. C., Álvarez-Herrero, A., et al. 2011, SoPh, 268, 57
Michel, E., Baglin, A., Auvergne, M., et al. 2008, Sci, 322, 558
Murabito, M., Guglielmino, S. L., Ermolli, I., et al. 2021, A&A, 653, A93
Noyes, R. W., Hartmann, L. W., Baliunas, S. L., Duncan, D. K., & Vaughan, A. H. 1984, ApJ, 279, 763
Pesnell, W. D., Thompson, B. J., & Chamberlin, P. C. 2012, SoPh, 275, 3
Pötzi, W., Veronig, A., Jarolim, R., et al. 2021, SoPh, 296, 164
Radick, R. R., Lockwood, G. W., Henry, G. W., Hall, J. C., & Pevtsov, A. A. 2018, ApJ, 855, 75
Radick, R. R., Lockwood, G. W., Skiff, B. A., & Baliunas, S. L. 1998, ApJS, 118, 239
Scargle, J. D., Keil, S. L., & Worden, S. P. 2013, ApJ, 771, 33
Scharmer, G. 2017, SOLARNET IV: The Physics of the Sun from the Interior to the Outer Atmosphere, 85
Scharmer, G. B. 2006, A&A, 447, 1111
Scharmer, G. B., Löfdahl, M. G., Sliepen, G., & de la Cruz Rodríguez, J. 2019, A&A, 626, A55
Scharmer, G. B., Narayan, G., Hillberg, T., et al. 2008, ApJL, 689, L69
Scherrer, P. H., Schou, J., Bush, R. I., et al. 2012, SoPh, 275, 207
Schmelz, J. T. 2003, AdSpR, 32, 895
Schou, J., Scherrer, P. H., Bush, R. I., et al. 2012, SoPh, 275, 229
Sheeley, N. R., J. 1967, SoPh, 1, 171
Sivaraman, K. R., Singh, J., Bagare, S. P., & Gupta, S. S. 1987, ApJ, 313, 456
Solanki, S. K., Barthol, P., Danilovic, S., et al. 2010, ApJL, 723, L127
Solanki, S. K., Riethmüller, T. L., Barthol, P., et al. 2017, ApJS, 229, 2
Sowmya, K., Shapiro, A. I., Witzke, V., et al. 2021, ApJ, 914, 21
Spruit, H. C. 1982, SoPh, 75, 3
Tsuneta, S., Ichimoto, K., Katsukawa, Y., et al. 2008, SoPh, 249, 167
van Noort, M., Rouppe van der Voort, L., & Löfdahl, M. G. 2005, SoPh, 228, 191
Wallace, L., Hinkle, K., & Livingston, W. C. 2005, An Atlas of Sunspot Umbral Spectra in the Visible from 15,000 to 25,500 cm^{-1} (3920 to 6664 Å) (Tucson, AZ: National Solar Observatory)
White, O. R., & Livingston, W. 1978, ApJ, 226, 679
White, O. R., Livingston, W. C., Keil, S. L., & Henry, T. W. 1998, in ASP Conf. Ser. 140, Synoptic Solar Physics, ed. K. S. Balasubramaniam, J. Harvey, & D. Rabin (San Francisco, CA: ASP), 293
Wilson, O. C. 1978, ApJ, 226, 379